Reviewed Preprint
v1 • November 5, 2025
Not revised

Reviewed Preprint
v2 • May 27, 2026
Revised by authors

For correspondence:
ujfalussy.balazs@koki.hun-ren.hu

Competing interests: No competing interests declared

Funding: See page 32

Reviewing editor: Christine Grienberger, Brandeis University, United States

Analysis of dendritic input currents during place field dynamics

Bence Fogel, Balázs B Ujfalussy

Biological Computation Research Group, HUN-REN Institute of Experimental Medicine, Budapest, Hungary

eLife Assessment

This study offers an **important** advance by extending an intuitive visualization tool that enables assessment of how dendritic and synaptic currents potentially shape neuronal output. The evidence supporting the tool's capabilities is **convincing**, with well-documented code, algorithmic innovation, and application to hippocampal pyramidal neurons. The work will be of interest to computational and systems neuroscientists seeking accessible methods to examine dendritic computations.

https://doi.org/10.7554/eLife.108352.2.sa3

Abstract

Neuronal activity is driven by the complex interplay between various membrane currents, often located in distinct domains of the spatially extended dendritic tree. How the effect of these currents propagates to the soma and contributes to neuronal output under in vivo conditions is not fully understood. Here, we develop a new method to measure and visualise the contributions of individual membrane currents to the somatic response in spatially extended biophysical model neurons. Our approach relies on the iterative decomposition of the axial current flowing between neighbouring compartments in proportion to the underlying membrane currents measured in the model. We apply this method to visualise the inputs driving hippocampal place cell activity. Our method provides a compact and intuitive description of the various dendritic events underlying subthreshold activity, spiking, or burst firing. By contrasting the dendritic input currents preceding spiking and bursting, we demonstrate that both could occur at highly variable input levels to proximal dendrites (basal and oblique), and that strong distal inputs facilitates, rather than controls, the generation of complex spike bursts. Our method opens a novel window onto single-neuron computations that will help to design better models and to interpret the results of in vivo imaging experiments.

Introduction

Characterizing the relationship between the dynamics of individual ion channels and the neuronal activity *in vivo* is crucial for mechanistic understanding of biological computation, to develop more realistic circuit models of brain activity, and to identify potential therapeutic targets.

Ion channels have been extensively studied both in isolation (Hille, 2001) and also in their interactions with other channels to explain the emergence of diverse neuronal activity patterns observed (Hodgkin and Huxley, 1952; Koch, 1999). A dominant view emerged that neurons form non-linear dynamical systems, with state variables corresponding to membrane potential (Vm), open probability of ion channel gates, and second messenger concentrations (Izhikevich, 2007). Even if the membrane currents are known, studying the impact of particular ion channels on the neuronal response in such a dynamical system under *in vivo* conditions is hindered by two major obstacles: First, synaptic inputs to neurons arrive in complex temporal patterns often engaging a combination of ion channels that interact with each other in potentially highly nonlinear, state-dependent manner. Measuring channel-contributions under *in vitro* conditions (Losonczy and Magee, 2006) or by pharmacological manipulations (Palmer et al.,

2014) may not engage the ion channels in the same way as during the high-conductance state *in vivo*, (Destexhe et al., 2003; Ujfalussy et al., 2018). In response to these challenges, the currentscape technique has recently been developed to provide an intuitive and simple way to visualize the high-dimensional current dynamics during naturalistic neural activity in one-compartmental biophysical neuron models (Alonso and Marder, 2019).

Second, synaptic inputs target the spatially extended dendritic tree of the neurons (Fig. 1B) where electrical and biochemical compartmentalization renders state variables local (Stuart and Häusser, 2001; London and Häusser, 2005; Branco and Häusser, 2010). With local state variables, the recruitment of ion channels can vary greatly between different dendritic domains (Häusser and Mel, 2003; Poirazi et al., 2003), which makes it especially difficult to understand or visualise current-interactions in neurons with a large dendritic tree under *in vivo* conditions. There are three simple ways to adapt the currentscape technique to neurons with realistic morphology: First, one could visualize the current dynamics in each compartment separately (Guet-McCreight and Skinner, 2020; Linaro et al., 2022). This strategy could work for few compartmental models but is clearly not feasible beyond a critical size and does not provide an intuitive description of the current propagation in neurons. Second, it is possible to sum up all membrane currents throughout the dendritic tree (Fig. 1A-D). However, this approach can not reveal the contribution of currents to the output of the cell, as even large-amplitude distal dendritic currents often fail to propagate to the soma (white arrowhead in Fig. 1D). Third, one could focus on a single compartment and study the input currents locally, for example at the somatic action potential generation site (Linaro et al., 2022). However, the dominant inputs are often currents flowing axially as a consequence of the activation of synaptic or intrinsic currents in other compartments (Fig. 1D). Here, we develop a computational technique, the *extended currentscape*, which is able to identify how membrane currents measured throughout the dendritic tree contribute to the axial current flowing into any particular compartment.

To demonstrate the ability of the extended currentscape method to provide an intuitive visualisation of input integration in neuron models with complex morphology under *in vivo*-like conditions, we apply it to study the generation of complex spike bursts (CSB) in hippocampal CA1 pyramidal neurons (PNs). In PNs CSBs are associated with Ca^{2+}-spikes in the apical dendrites (Larkum et al., 1999; Grienberger et al., 2014; Magó et al., 2021) and are believed to play a critical role in learning (Payeur et al., 2019) and memory formation (Bittner et al., 2015, 2017; Grienberger and Magee, 2022; Wen et al., 2024). However, the precise role of the different input pathways in triggering Ca^{2+}-spikes in these cells remained unclear: On the one hand, Ca^{2+}-spikes can be readily initiated by distal dendritic, but not by somatic current injection *in vitro* (Golding et al., 1999; Takahashi and Magee, 2009), the timing of the Ca^{2+}-spikes coincides with inputs to the most distal branches during theta oscillation (Bittner et al., 2015) and blocking entorhinal inputs decreases the probability of CSB firing (Bittner et al., 2015) all emphasizing the critical role of distal inputs in controlling CSBs. On the other hand, CSBs can be triggered by somatic current injection in most PNs at random spatial locations *in vivo* (Bittner et al., 2015, 2017) or *in vitro*, after blocking dendritic potassium channels (Bittner et al., 2017), distal inputs alone are not as effective as combined with proximal inputs in triggering CSBs (Takahashi and Magee, 2009) and distal tuft dendrites are variably recruited during putative CSB events *in vivo* (O'Hare et al., 2025), raising the possibility that proximal inputs also play an important role in the initiation of CSBs.

In this paper, we first describe the *extended currentscape* technique that generalizes the standard currentscape visualization method to neurons with spatially extended dendritic trees. We show that the extended currentscape accurately and intuitively captures the origin and type of dendritic events in models with simplified or realistic morphology under spatially localised synaptic stimulation conditions. Next, we analyse the membrane currents and the Vm dynamics of a biophysical model CA1 PN showing place cell-like activity. We show that the membrane potential throughout the entire dendritic arbor has low-dimensional dynamics dominated by global activity even when localised dendritic events are abundant in distal dendrites. Next, we analyze CSBs in the model using the extended currentscape method and show that they can be started with highly

Fig. 1. Challenges in identifying the biophysical factors underlying neural responses.

A) Somatic Vm response of a biophysical model CA1 pyramidal neuron to distributed naturalistic synaptic inputs. Blue box highlights the portion analyzed in panel C. **B**) Morphology of the simulated neuron with the location of the synapses (green: excitatory; blue: inhibitory synapses; dark green indicates the location of 12 functional synaptic clusters. See Methods and Fig. 4 for more details.) **C**) Magnified part of the somatic Vm response. Filled arrowhead highlights a spikelet. **D**) Visualising the input currents in the model using the currentscape technique (Alonso and Marder, 2019). Top: the magnitude of the total inward current on a logarithmic scale. Since we included the capacitive current to the sum (Eq. (1)), the magnitude of the inward and the outward currents is identical (Kirchhoff's law). Here membrane currents across the entire dendritic tree were summed. Bottom: Percentage of the different ion channels, including intrinsic and synaptic channels, contributing to outward (inhibitory, top) and inward (excitatory, bottom) currents. Color legend is shown on the right and applies to all subsequent figures. White arrowhead indicates a large Ca^{2+}-current that does not appear in the somatic Vm response. Filled arrow highlights dendritic Na^{+}-channel activation corresponding to spikelet in C. **E**) Currentscape applied to the somatic currents including currents flowing axially from different dendritic branches (grey).

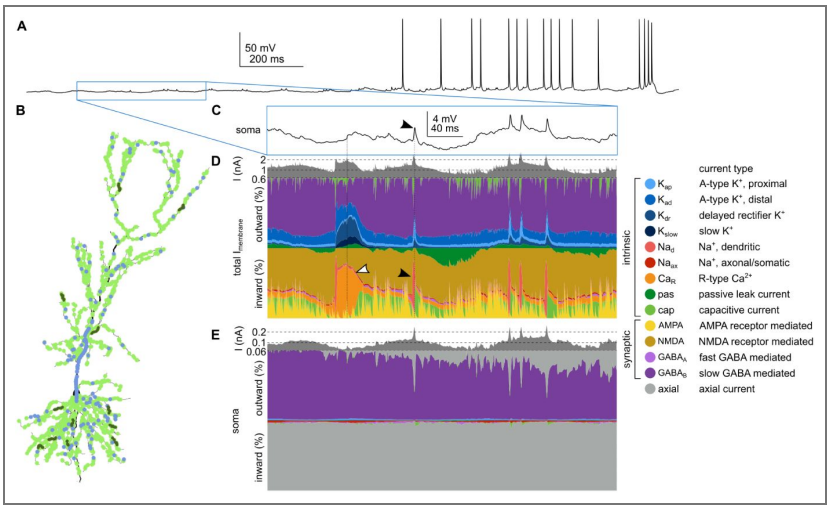

Table 1. Glossary

compartment	Colloquial term for a morphological unit in a biophysical, multicompartmental model (e.g., soma or a dendritic branch)
section	A continuous length of unbranched cable in a multicompartmental model.
segment	Smallest spatial unit in a multicompartmental model that is isopotential and uniform in its properties. It corresponds to a *node* in the connectivity graph. To calculate the extended currentscape, we need to record the membrane currents in all segments and axial current between all connected segment pairs.
connectivity graph	Graph representation of the multicompartmental model; it ignores 3D position of the nodes, or their diameter.
node	Representation of a segment in the connectivity graph. Membrane current flows in or out of the cell at the nodes.
edge	Nodes connected with edges represent neighbouring segments along the cable. Axial current flows along the edges in the cell.
target node	The final target of the partitioning algorithm. Any node can be selected for being the target node. Once selected, it becomes the root of the tree, where the pruning starts and the partitioning ends.
child node	For partitioning the axial current between a pair of nodes, the node that is *further away* from the target is the child node.
parent node	For partitioning the axial current between a pair of nodes, the node that is *closer* to the target is the parent node.
pruning	A process where continuous flow of axial current from distal nodes towards the target are identified and the rest of the graph is removed. Repeated in each time step.
collision node	A node where the direction of axial currents change.
collision edge	The first edge after the collision node with altered axial current direction.

variable initiation dynamics. By contrasting CSBs and isolated single spikes, we reveal that although distal inputs facilitate the generation of CSBs, there is no need for exceptionally strong tuft inputs nor Ca^{2+} hotspots for their initiation.

Results

The extended currentscape method

We start by describing the extended currentscape visualization method which aims to capture how membrane currents in a distant *reference* (e.g., dendritic) compartment influence the activity of a *target* (e.g., soma) compartment. Our method relies on the equivalent circuit model of neurons (Koch and Segev, 2000) and requires measuring the membrane and axial currents throughout the dendritic tree of a neuron (in every node of the circuit) to partition the axial currents flowing into the target compartment by the underlying membrane currents. Since this kind of data is not available in real neurons, we used multicompartmental biophysical models (Jarsky et al., 2005; Ujfalussy and Makara, 2020) to develop and test our method. With the advent of novel single-neuron voltage imaging techniques (Brooks et al., 2024; Liao et al., 2024; Park et al., 2025; Lee et al., 2026), our method could potentially also be adapted to data from real neurons in the near future.

The intuition behind our method is that distant currents can directly influence the Vm of the target compartment only if there is a continuous flow of axial current from reference to target, i.e., if the axial current is not blocked or reversed between the reference and the target. In order to characterise the relationship between the axial currents and the membrane currents we start with Kirchhoff's current law, stating that the sum of all currents flowing into or out of a node in an electrical circuit must be zero. Applying it to a small segment of a neuronal process, we have:

$$C\frac{dV_m(t)}{dt} + \sum_i I_i^{\mathrm{mem}}(t) + \sum_j I_j^{\mathrm{ax}}(t) + I_{\mathrm{inj}}(t) = 0 \quad (1)$$

Here C is the membrane capacitance, $C\frac{dV_m(t)}{dt}$ is the capacitive current, I^{mem} denotes the membrane currents, including all synaptic and intrinsic currents, I^{ax} denotes all axial currents flowing from the neighbouring segments and I_{inj} is the current injected into the cell through a stimulation electrode. Eq. (1) states that if the axial current flows from the target towards a child node (as at t_1 in Fig. 2A), then the sum of the outward currents must be larger than the sum of the remaining inward currents in the child compartment. In this case, we postulate that this excess outward current is responsible for the axial current flowing towards the child compartment, and we partition the axial current in the proportion of the outward currents in the child compartment (Fig. 2B, left). In contrast, when the direction of the axial current between the child and the target reverses (Fig. 2A, t_2), we partition it proportionally to the inward currents in the child compartment (Fig. 2B, right). Note that the sign of membrane currents can also reverse when the membrane potential crosses their reversal potential. In our simulations this often happened with the leak current, which had its reversal potential (E_{leak} = −66 mV) between that of excitatory (E_{NMDA} = 0 mV) and inhibitory inputs (E_{GABA} = −80 mV). This way, the same current type can contribute to inward or outward axial currents at different time points or in different compartments.

Fig. 2A-C illustrates the application of the extended currentscape to a simple biophysical model in which synaptic input to the dendrite evokes an EPSP that propagates to the soma. As we want to analyse the currents driving the soma, we choose the soma to be that target compartment throughout the analysis (the user can pick any compartment to be the target but it remains the target throughout the analysed time period). In this model, small baseline Na^+-current makes the soma more depolarized than the dendrite in the equilibrium, and the axial current flows outward from the target compartment (Fig. 2A-B, t_1). After the input is activated, the axial current

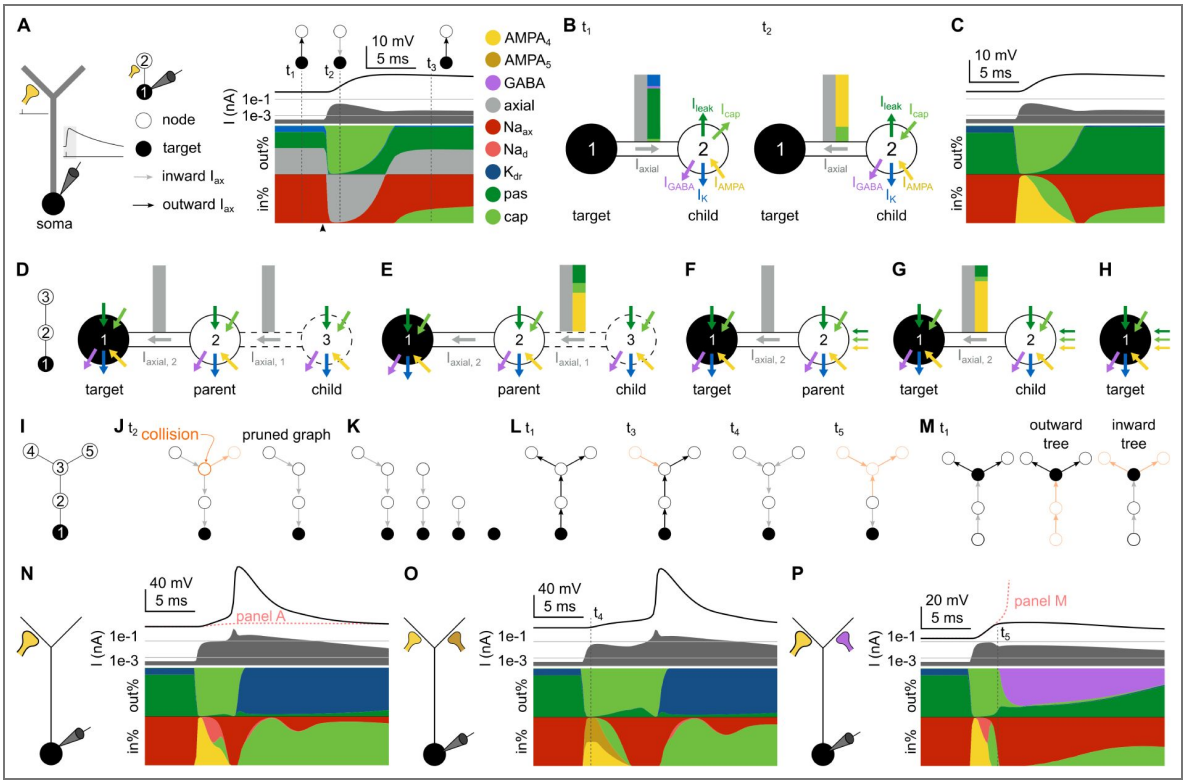

Fig. 2. Partitioning the axial current.

A Currentscape analysis of a simple model responding to excitatory synaptic input. Left: Morphology of the model with a soma, an apical trunk and two dendritic branches. Insets show the stimulus and the somatic response, with the period analysed in later panels highlighted. Middle: simplified graph representation of the model with two nodes. Here we used this 2-node graph only for illustration purposes. See panels D and I for larger graphs describing the same biophysical model. Right: currentscape of the somatic compartment of the model. Vertical dotted lines indicate the time points analysed in panels B, J and L, with the corresponding axial current directions shown as insets; arrowhead show the timing of the input. pas: passive leak current. cap: capacitive current. **B**) The axial current of the *target* compartment (grey arrow) is partitioned by the membrane currents in the *child* compartment (coloured arrows). When the axial current flows away from the target, it is partitioned by the outward currents in the child (t_1, left). When the direction of the axial current reverses, it is partitioned by the inward currents in the child (t_2, right). **C**) Extended currentscape of the somatic node shown in panel A. **D-H**) Partitioning recursion. Partitioning begins at the most distal child compartment (3) and moves through its parent towards the target (e.g., 1–soma; D). In the first step, $I_{\text{axial},1}$ is partitioned proportionally to the inward currents in node 3 (E). Next, the partitioned axial currents are added to the membrane currents in the parent (node 2; F). Steps D-F are repeated for the next pair of nodes (F-G) until the target is reached. **I-L**) Iterative partitioning in a graph. **I**) Graph representation of a multicompartmental model. The compartments (nodes) are denoted by circles and the axial current flow is indicated by arrows (edges). **J**) The graph, representing the flow of axial currents at t_2 in panel A is pruned at the *collision* edges, where the direction of the axial current reverses. **K**) Partitioning algorithm starts from a leaf node and progresses towards the target. **L**) The structure of the pruned graph is time dependent: each graph shows a pattern of axial current flow at different time points from panels A, O or P. Orange colours highlight the part of the graph behind the colliding edge that can not directly contribute to axial currents towards the target. **M**) Partitioning with node 3 as the target: inward and outward currents are considered separately for both pruning and partitioning. **N-P**) Currentscape analysis of the responses of the simple model to strong synaptic input evoking a dendritic Na^+-spike triggering a somatic AP (N), coincident excitatory inputs to different dendritic branches (O) and inhibitory input blocking somatic AP after a dendritic Na^+-spike (P).

reverses and depolarizes the soma giving rise to the measured EPSP (Fig. 2A-B, t_2). During the repolarization phase (Fig. 2A, t_3) the axial current returns to its original direction flowing from the soma towards the dendrites. The extended currentscape plot reveals that the somatic depolarization was mainly caused by synaptic AMPA receptor mediated currents (yellow in Fig. 2C), while the outward currents left the cell via leak currents (dark green in Fig. 2C).

In a multicompartmental model, the partitioning of the axial currents can be applied iteratively starting from the most distal compartment and proceeding towards the target once all axial currents arriving at the parent from the more distal nodes had been partitioned (Fig. 2D-E). In the next step, the partitioned axial currents are added to the membrane currents in the parent node (Fig. 2F) before moving one step closer to the target (Fig. 2G-H).

In general, the topology of the model is represented by an acyclic graph, where each node is a segment, the directed edges represent the flow of the axial current and the root node of the graph is the target (Fig. 2I-L). Partitioning starts with following the flow of axial currents from the target towards the leaf nodes of the tree. The nodes where the direction of the axial current is reversed are collision points (Fig. 2J). Since the propagation of the axial current is blocked at the collision points, the membrane currents of the nodes distal to the colliding edge do not have a direct influence on the activity at the target. Therefore, to make the algorithm computationally more efficient, in every time step we prune the graph at collision edges and apply the partitioning recursion only to the pruned graph (Fig. 2J-K). Since the direction of the axial currents often changes during the simulations, the shape and size of the remaining graph can vary between different time points (Fig. 2L). The target node may connect multiple subtrees, and the axial currents of the subtrees are pruned and partitioned separately (Fig. 2M).

After partitioning the axial currents of the target compartment we can use the standard currentscape plot (Alonso and Marder, 2019) to visualize the contribution of distal membrane currents to the mem-brane potential dynamics of the target. The entire process must be repeated when a new target compartment (e.g. a dendritic branch) is selected (Fig. 2M). Throughout the paper, we will use two different variants of the partitioning algorithm: we will either partition axial currents by the *type* of membrane currents (e.g., current flowing through Ca^{2+} or Na^{+} channels) or by the dendritic *region* of the reference compartments (i.e., basal, oblique or tuft dendrites). However, alternative variants of the partitioning algorithm can also be devised (see Methods).

To illustrate how the extended currentscape analysis can provide a compact summary of the distal currents driving the somatic response in simple, intuitive situations, we show three additional examples (Fig. 2M-O). First, we increased the distal synaptic conductance, which now evoked a local dendritic Na^{+}-spike (Fig. 2M), and the somatic EPSP became large enough to trigger an action potential (AP). Similarly, if two weak synapses are stimulated coincidentally at different dendritic branches, their combined activation can also lead to a somatic AP (Fig. 2N). Although the axial currents arriving to the soma are similar in these cases, the extended currentscape can reveal the differences in the membrane dynamics leading to the somatic spikes. Finally, off-the-path inhibition can prevent the generation of the somatic AP triggered by the local dendritic spike (Fig. 2O). In this case, the strong, GABA-receptor mediated outward currents are visible on the currentscape plots during the repolarization phase of the EPSP.

Next, we will apply the extended currentscape technique to analyze input integration and the mechanism of burst firing in hippocampal place cells.

Currentscape analysis of dendritic integration in the CA1 pyramidal neuron model

To study the synaptic input conditions that lead to burst firing under *in vivo*-like conditions we used a previous CA1 PN model containing Na^{+}-channels, a delayed rectifier K^{+} channels and two variants of A-type K^{+}-channels in basal and apical dendrites (Jarsky et al., 2005; Ujfalussy and Makara, 2020) and extended it with a minimal set of channels necessary for the generation of complex spike bursts. Experimental data indicates that R-type Ca^{2+}-channels are mainly

responsible for both burst firing and for dendritic plateau potentials in this cell type (Magee and Carruth, 1999; Metz et al., 2005; Takahashi and Magee, 2009). We used a novel Ca^{2+}-channel model that displayed similar activation and inactivation kinetics to the Ca^{2+} currents recorded in the apical dendrites in CA1 PNs (Fig. S1A; Magee and Johnston 1995) and distributed it uniformly across all apical dendrites (trunk, obliques, and tuft) of the cell (Magee and Johnston, 1995; Poirazi et al., 2003).

Various potassium channels contribute to the repolarization after Ca^{2+}-spikes, including Ca^{2+}-activated potassium channels (Golding et al., 1999; King et al., 2015), but the precise biophysical characterization of these channels is currently lacking. To model their overall effect, we used a high voltage activated potassium current with relatively slow kinetics (Fig. S1B) in the apical dendrites.

Equipped with these channels, our model was able to fire a short burst of 3-4 action potentials with decreasing amplitude riding on a depolarizing wave upon dendritic current injection (Fig. S1C). These somatic bursts were accompanied by dendritic Ca^{2+}-spikes, so we refer to them as complex spike bursts or CSBs. In agreement with the experimental data (Golding et al., 1999) the model had a lower threshold for initiating Ca^{2+}-spikes in the apical trunk than in the soma (Fig. S1D). Under *in vivo*-like synaptic input conditions (see below and Methods), dendritic Ca^{2+}-spikes could also be evoked by somatic current injection (Fig. S1E), as in Bittner et al. (2015).

To illustrate the ability of the extended currentscape method to provide a compact and intuitive summary of dendritic events in the model, we first tested it under simple, spatially and temporally restricted input conditions. We first used the model without dendritic Ca^{2+}-channels and stimulated an increasing number of synapses in a single oblique branch Fig. 3A-C). We found that the somatic response became superlinear beyond a branch-specific threshold, with a sigmoid superlinearity (Fig. 3A-B), reminiscent of experimental findings with 2-photon glutamate uncaging (Losonczy and Magee, 2006). Partitioning the somatic currents by the current type (Fig. 3C, middle) indicated that before stimulation, the inward currents were mainly leak currents (dark green), with some contribution from the somatic and axonal Na^{+}-currents (red). Partitioning the somatic currents by the region of their origin (Fig. 3C, bottom) showed, that current flew from the axon and basal dendrites towards the soma and further towards the apical dendrites, that were more hyperpolarized than the soma due to the larger density of K^{+} channels in the apical trunk. Upon stimulation, the inward currents show first a fast, AMPA-mediated and later a slower NMDA-mediated component (yellow and olive in Fig. 3C, middle), both originating from the stratum radiatum (levander in Fig. 3C, bottom). At n=20 inputs a Na^{+}-spike that remains local to the stimulated branch is responsible for the spikelet appearing in the somatic response (pink in Fig. 3C, right). During these events, the inward current arrived transiently from the apical dendrites (see shades of levander in Fig. 3C, bottom), and left the soma towards the basal dendrites (pink in Fig. 3C). At the end of the events the NMDA contribution disappeared from the soma as the axial current reversed to its original direction, flowing from basal towards apical dendrites.

Next we repeated the same stimulation protocol after including the Ca^{2+}-channels to the apical dendrites of the neuron. The addition of the Ca^{2+}-channels rendered the shape of the superlinearity more step-like, as in single-photon uncaging or synaptic stimulation experiments (Fig. 3D-E; Wei et al. 2001; Ariav et al. 2003; Cai et al. 2004). Under these conditions the combined Ca^{2+}- and NMDA-spikes did not lead to somatic action potential firing but remained localised to the stimulated branch. The currentscape analysis revealed that activation of Ca^{2+}-channels first boosted the NMDA currents activated at near-threshold responses (at n=10 inputs, orange in Fig. 3F), and were further amplified by local Na^{+}-spikes (at n=15 or 20 inputs; Fig. 3F). During these events, NMDA-mediated and Ca^{2+}-currents contributed similarly to the somatic depolarization (Fig. 3).

Taken together, these simulations confirmed that extended currentscapes provide a rich form of visualization of the sequence of dendritic events leading to somatic responses even in cells with complex morphology under relatively simple input conditions. Next, we used this model to investigate the synaptic input patterns leading to CSB firing during *in vivo*-like inputs.

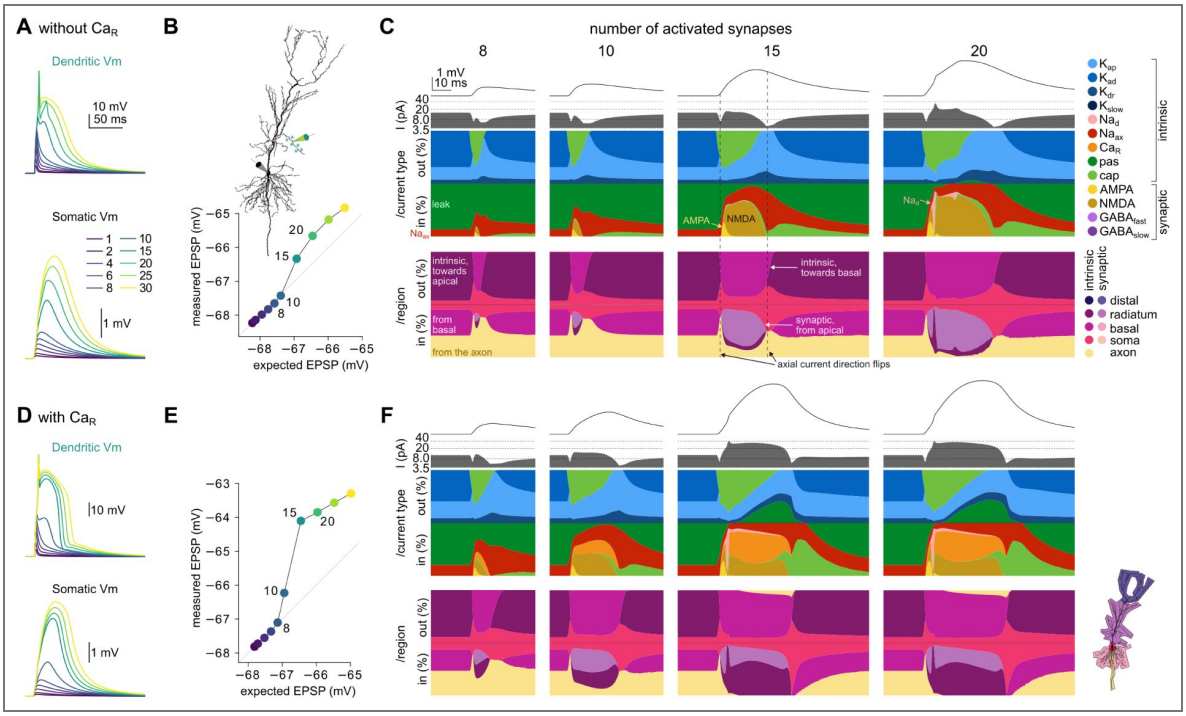

Fig. 3. Currentscape analysis of dendritic integration in the CA1 PN model.

A) Dendritic (top) and somatic (bottom) Vm in response to stimulating an increasing number of synapses (N=1-30) on an oblique dendrite (inset in B) with 0.3 ms delay in the model without Ca^{2+}channels. Note the fast dendritic Na^{+}-spike appearing at n=20. **B**) Expected versus measured somatic response amplitude of the stimulations shown in A. Inset shows the branch used for stimulation and dendritic recordings. **C**) Extended currentscape analysis of the somatic responses to an increasing number of stimulations (n=8, 10, 15 and 20 shown). Top line: somatic membrane potential (Vm) response. Second line: total outward membrane current on log-scale. Third line: percentage of somatic outward and inward currents partitioned by the current type. Fourth row: somatic currents partitioned by the current origin. **D-F**) Same as A-D for the model equipped with Ca^{2+}-channels in the apical dendrites. Note the step-like response in the dendritic Vm (D, bottom) and the large Ca^{2+}-currents for n=15 and 20 stimuli (F, right).

CSBs in the CA1 pyramidal neuron model

To create place cell activity in response to *in vivo*-like input condition we simulated the activity of 2000 excitatory and 200 inhibitory presynaptic neurons during the traversal of a 2 m long linear track as de-scribed previously (Fig. 4A; Ujfalussy and Makara 2020; Kim et al. 2023). Briefly, each excitatory neuron had a ~ 20 cm long place field and neurons showed theta modulation and displayed phase precession (Skaggs et al., 1996). Place fields were distributed uniformly across the linear track. The majority of the 2000 excitatory synapses were placed randomly on the dendritic tree (avoiding the soma and the proximal apical trunk; light green in Fig. 1B), while the remaining 240 inputs active in the middle of the track were organized into 12 functional synaptic clusters (Adoff et al., 2021) where presynaptic neurons with similar place fields (dark green circles in Fig. 4A) innervated neighbouring dendritic locations (Fig. 1B; Adoff et al. 2021) and had larger synaptic conductance (see Methods; Bittner et al. 2015; Heredi et al. 2025). These synaptic clusters provided strong drive to the cell in the middle of the track by activating a few dendritic branches (Ujfalussy and Makara, 2020).

Inhibitory neurons showed theta modulation (Csicsvári et al., 1999) but were spatially untuned (Wilson and McNaughton, 1993; Dupret et al., 2013) consistent with their indirect role in shaping spatial selectivity in place cells (Grienberger et al., 2017). Half of the inhibitory cells targeted the soma and the proximal apical trunk, the other half was randomly distributed throughout the dendritic tree (blue circles in Fig. 1B; Megias et al. 2001).

First, we analyzed the somatic and dendritic Vm response of the model. The neuron responded to synaptic stimulation with a train of action potentials in the middle of the simulated track consisting of a variable number of single spikes and CSBs (Fig. 4B). During CSBs the distal apical dendrites showed a Vm response similar to the Ca^{2+}-spikes observed *in vitro* (Fig. 4B, bottom trace). In a set of 16 simulations with variable cluster placement and synaptic input patterns, the Vm of the entire neuron was highly correlated (Fig. 4C), with a single factor explaining ~70% of the total variance across the dendritic branches (Fig. 4D, Lee et al. 2026). The weights associated with this first factor uniformly covered the entire dendritic tree (Fig. 4E, see also Fig. S2) indicating the dominance of the global modulation of the dendritic Vm mainly due to back-propagating action potentials (bAPs, Spruston et al. 1995). In contrast, the weights associated with the second principal component had an opposite sign perisomatically versus distally, demonstrating a greater level of independence from the soma in distal tuft branches (Fig. 4E).

When we inspected the dendritic Vm during CSBs we found that in our model CSBs were not preceded by large, global Ca^{2+}-spikes in the tuft. Instead, dendritic Ca^{2+}-spikes typically started asynchronously (O'Hare et al., 2025), often after a back-propagating action potential or a local Na^{+}-spike (Fig. 4F, see more examples in Fig. S3; Park et al. 2025; Lee et al. 2026). Although in distal dendrites we could observe local Na^{+} or Ca^{2+}-spikes not coupled to somatic activity (see below in Fig. 5), local dendritic Vm peaks closely followed somatic APs in the majority of cases (>90%; Fig. 4G). When we analysed the spatial extent of the dendritic events, we found two distinct clusters Fig. 4H): most (90%) of the events were local, restricted to a small subtree (< 20, μ = 1.8 branches). These local events occurred in higher-order (mostly terminal) basal or apical branches (Fig. 4I). The second group was associated to bAPs reaching the majority of the dendritic branches, with propagation failures occurring mainly in higher-order apical dendrites beyond 200 μm from the soma (Fig. 4J; Lee et al. 2026). This way, although only 10% of the dendritic Vm events were associated with bAPs, they reached ~60-times more branches than local events and they dominated the PCA analysis even in the presence of local regenerative dendritic events driven by strong, functionally clustered synaptic inputs.

Currentscape analysis of place field dynamics

To better understand how individual dendritic events influenced the somatic response of the cell, we calculated the extended currentscape of the simulated neuron in the time window around its activity in the place field (Fig. 5), and analysed the membrane currents at subthreshold activity (Fig. 5B), AP firing (Fig. 5C) and during complex spike bursts (Fig. 5D). Partitioning the

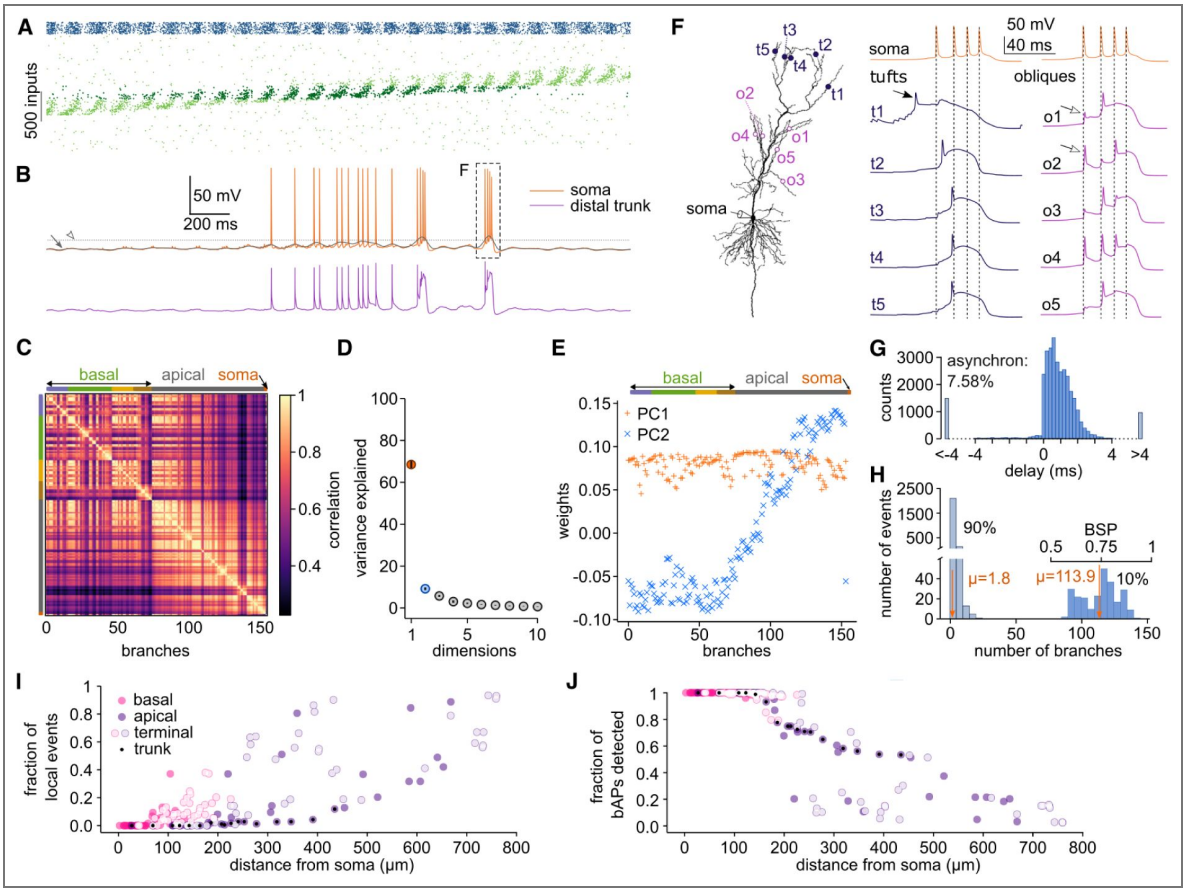

Fig. 4. Model response to complex synaptic inputs.

A) Activity of the 2000 excitatory (green; ordered by the place field location) and 200 inhibitory synapses (blue). Note the theta oscillation and the theta sequences in the excitatory inputs. Synapse locations are shown in Fig. 1B. Dark green indicates the 240 excitatory synapses with stronger weights and organized to functional clusters (see Methods). **B**) Somatic (top) and dendritic (from distal apical trunk, bottom) Vm response of the model to the synaptic input pattern shown in A. Grey line (arrow) shows the filtered somatic Vm response used to detect complex spike bursts (CSB). CSBs coincided with large depolarizing events in the dendrite. Dotted line (empty arrowhead): CSB detection threshold. The second CSB event (box) is analyzed further in panel F. **C**) Average (n=16 laps) cross-correlation of the Vm of the 153 dendritic branches in the model. Branches are ordered by morphology of the cell, not by correlation strength. Soma is shown as branch 153. **D**) The correlation matrix is low rank: the first two components (orange and blue) explain ~80% of the variance of the Vm. Error bars show SD across 16 simulations. **E**) The weights of the first two principal components (PC1 and PC2) in an example simulation: the first component describes a uniform activity across the entire cell, while the second captures activity differences between the perisomatic region and distal apical dendrites. **F**) Left: location of the dendritic Vm recordings (t: tuft, o: oblique, s: soma). Right: Dendritic Vm during somatic burst firing. Filled arrow indicates a local dendritic Na^+ spike, open arrows highlights backpropagating APs. **G**) Histogram of the time difference between dendritic Vm peaks (reaching -30 mV, with a prominence of 30 mV) and the closest Vm peak at the soma, calculated from 16 simulations and the 153 dendritic branches. **H**) Histogram of the spatial extent of each dendritic event. The 90% of the events were local (light blue), involving < 20 branches (μ = 1.8). The remaining 10% (dark) were associated with somatic APs. Branch spike prevalence (BSP) of these events is shown on the top. **I-J**) Fraction of local events (I) and fraction of bAPs detected as a dendritic event (J) as a function of the distance of the branch from the soma. Light color: terminal branches; black dot: apical trunk.

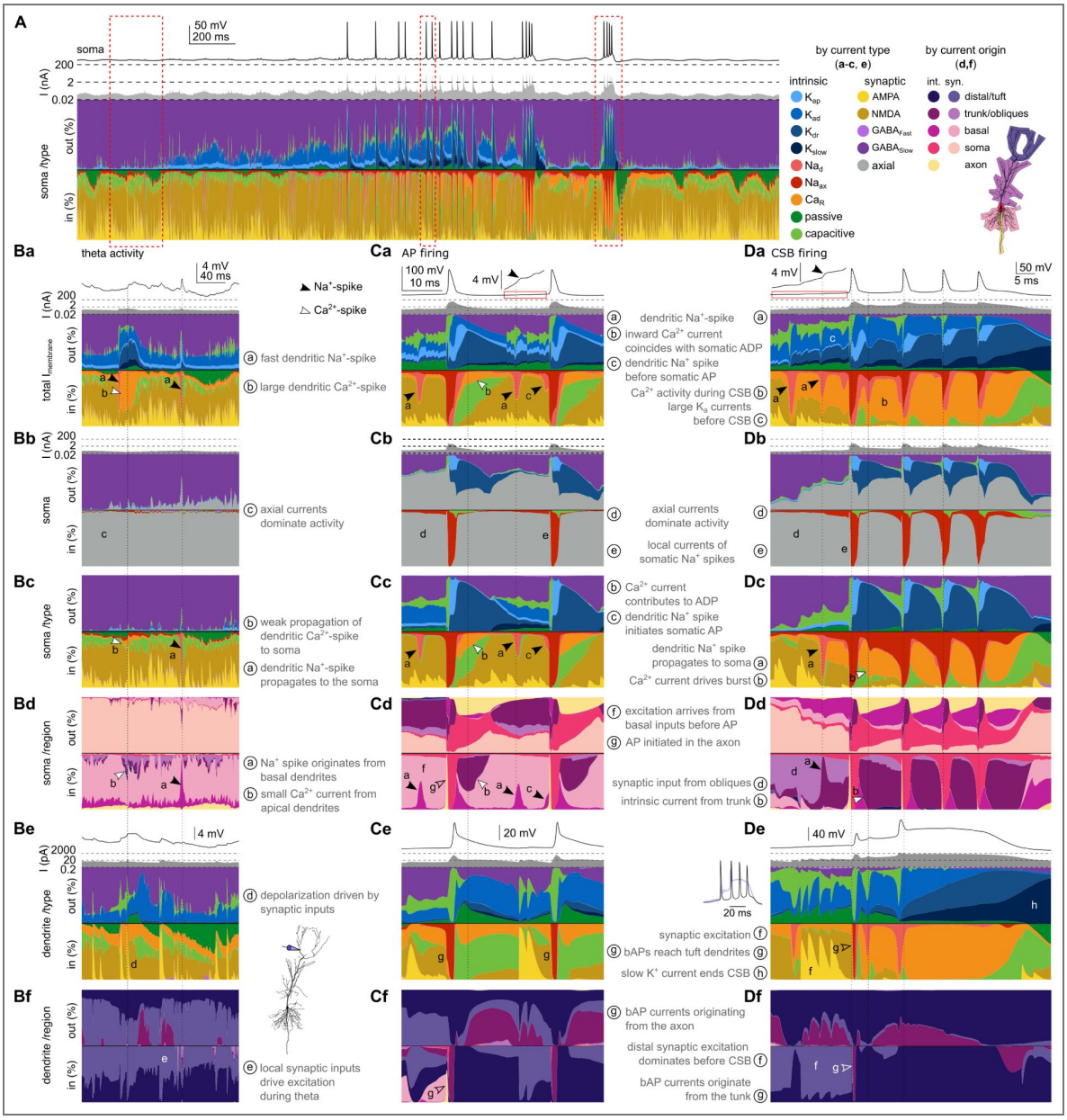

Fig. 5. Current dynamics in a place cell.

A) From top to bottom: Somatic Vm; inward somatic currents (log scale) and percentage of different outward and inward currents. Colour legend is shown on the right. Red boxes highlight temporal intervals analyzed in panels B-D. Filled arrowheads in panels B-D indicate local dendritic Na^+-spikes, open arrowheads point to bAPs and white arrowheads highlight Ca^{2+}-spikes. **B**a-f) Current dynamics outside of the place field. **B**a) Total membrane current of the cell during theta oscillation. **B**b) Somatic currents, including currents flowing from dendrites (axial currents, grey). **B**c) Somatic currents partitioned by current type. White arrowhead highlights that dendritic Ca^{2+}-spike has very little contribution. **B**d) Somatic currents partitioned by current source region. Colour legend is shown on the right of panel A. Arrowheads highlights that Ca^{2+}-spike originated in the apical region whereas the Na^+-spike came from a basal dendrite. **B**e) Membrane potential (top), sum of inward currents (middle) and input current types in a tuft branch. The recording location is shown as an inset next to panel Be. **B**f Tuft currents partitioned by current region. **C**a-f) Same as panel B during action potential (AP) firing. Dendritic Na^+-spikes originating in the basal dendrites (Cd) appear as spikelets in the soma (filled arrowhead; inset in Ca). The cell is mostly driven by NMDA inputs (Cc) targeting basal dendrites (Cd) and the tuft is largely decoupled from the rest of the neuron, though APs back-propagate (open arrowhead in Cf). **Da-Df**) Same as panel B during CSB firing. CSB is preceded by multiple dendritic Na^+-spikes, some propagating to the soma (black arrowhead in Dc) from stratum radiatum dendrites (Dd). This facilitates a Ca^{2+}-spike from the oblique-trunk region to propagate to the soma (Da-Dd) leading to the first somatic AP. The back-propagating AP (open arrow in Df) triggers Ca^{2+}-spike in tuft and oblique branches that efficiently propagates to the soma and triggers CSB (white arrowhead in Dc and Dd). Further details are in the legend.

somatic axial currents by current type revealed that before entering the place field, the cell was driven mainly by synaptic currents (Fig. 5Ba-c). Voltage dependent Na^+ or Ca^{2+} channels only activated occasionally and briefly, and their effect often remained localized, not being able to efficiently propagate to the soma (Fig. 5Ba-c). When the effect of dendritic Na^+-spikes reached the soma, they either appeared as small spikelets (Fig. 5Ba) or as fast rise in the somatic Vm (Fig. 5Ca). Partitioning the somatic axial currents by their origin indicated that, in this simulation, the soma was driven mainly by the basal dendrites (Fig. 5Bd). Performing similar partitioning of the axial currents in the tuft by their type (Fig. 5Be) and by their origin (Fig. 5Bf) revealed that the tuft region was driven by local synaptic currents and was largely decoupled from the rest of the cell.

Within the place field, somatic action potentials were evoked directly by synaptic inputs (first AP in Fig. 5C) or triggered by Na^+-spikes propagating from nearby basal dendritic branches (second AP in Fig. 5C). At the beginning of the action potential, a brief current originating from the axon can be observed (Fig. 5Cd), indicating that APs are initiated in the axon. In our model, active backpropagation of the APs is limited to the apical trunk, since the Na^+-channels in the higher order dendritic branches have a higher voltage threshold (Ujfalussy and Makara, 2020). Indeed, back-propagating APs do not recruit local, dendritic-type Na^+-channels in the tuft (Fig. 5Ce). In contrast, Ca^{2+}-currents are recruited in the apical dendrites and contribute to the spike after depolarization (Fig. 5Ca-f).

The model neuron also fired complex spike bursts (CSBs) within its place field (Fig. 5D). When we magnified the current dynamics around the second CSB, we found that it was preceded by strong Ca^{2+}-currents and dendritic Na^+-spikes that eventually reached the soma and elicited a somatic AP (Fig. 5Da-d). In this case, the cell was driven by a mixture of synaptic and intrinsic inputs from the apical dendrites already before the CSB (Fig. 5Dd). The first AP propagated back to the dendrites and amplified the dendritic Ca^{2+}- and Na^+-currents (Fig. 5Db-d). These intrinsic currents, originating from the apical dendrite, became the dominant inward drive in the soma and drove the cell to fire further APs (Fig. 5Db-d) until the slow potassium current in the dendrites terminated the burst (Fig. 5De-f). Taken together, the extended currentscape plots provide compact and intuitive visualization of the complex current dynamics underlying neuronal activity during spatially and temporally structured synaptic inputs in single trials. Next, we set out to systematically study the conditions leading to CSB firing in our model.

Input conditions for complex spike burst generation

To identify the input conditions leading to complex spike burst firing in our model, we focused on 41 CSB events from 16 simulations with different cluster location and input patterns, and contrasted them with 58 isolated action potentials (iAP; no other APs within 30 ms). First, we focussed on the membrane potential dynamics in long (>60 μm) terminal branches in the basal, oblique or tuft region. We found that during CSBs the Vm was highly variable across events, but was typically substantially depolarized for ~40 ms in both tuft and oblique dendrites (Fig. 6A), indicating the presence of dendritic Ca^{2+}-spikes in these branches. The large depolarizations associated with local Ca^{2+}-spikes were absent in basal dendrites or during iAPs (Fig. 6A-B).

Interestingly, the depolarization started earlier in the tuft than in the oblique branches, where it reached its maximum level only after the second AP in the burst. During CSBs most tuft branches participated in Ca^{2+}-spike firing (Fig. 6C), whereas the prevalence of dendritic Ca^{2+}-spikes remained low during isolated spikes (Fig. 6D). In the tuft branches, but not in obliques, both the mean Vm and the probability of Ca^{2+}-spikes diverged between CSBs and iAPs already ~10 ms before the start of the event (Fig. 6B,D). Note that the synapse density, the ion channel mechanisms and the input statistics were identical for tuft and oblique branches, suggesting that the morphology of the cell could be a primary factor underlying the increased excitability of the tuft for Ca^{2+}-spikes.

To more directly test the involvement of tuft dendrites in CSB generation, we compared the location of active synaptic clusters during CSBs and iAPs. We found that the average cluster distance from the soma was significantly larger during CSBs than iAPs (Fig. 6E). These

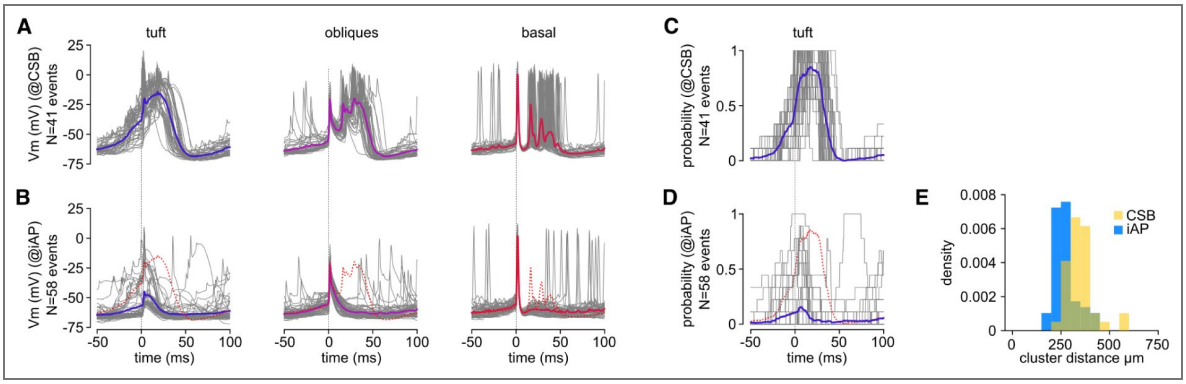

Fig. 6. Dendritic Vm dynamics during CSBs and isolated spikes.

A) Average dendritic Vm at somatic CSB firing. Grey lines show average across several branches in a given dendritic domain (tuft, obliques and basal dendrites) during individual CSB events; coloured lines show average across 41 CSB events. **B**) Average dendritic Vm at temporally isolated action potentials (iAPs) in different dendritic domains. Coloured lines show average across 58 events. Dotted red line shows the average response to CSB. **C-D**) Probability of Ca^{2+}-spikes in tuft dendrites aligned to the start of CSBs (C) or isolated somatic spikes (D). **E**) Mean path distance of the active synaptic input clusters from the soma during CSBs and isolated spikes (t-test: $p = 10^{-5.98}$).

observations confirm earlier results suggesting the special importance of tuft branches in controlling CSBs in CA1 neurons (Takahashi and Magee, 2009; Bittner et al., 2015; Grienberger and Magee, 2022; Park et al., 2025).

To further analyze the synaptic and dendritic events leading to CSB firing, we turned to our extended currentscape method and calculated the average currentscapes for both CSBs and iAPs (Fig. 7A-B). The somatic currentscapes by current type and current origin revealed the strong Ca^{2+}- and Na^{+}-currents driving burst firing in the soma during CSBs and being responsible for the slight depolarization after iAPs. However, to our surprise, there was almost no difference between CSBs and iAPs until the end of the first spike neither in the magnitude, nor in the origin or the composition of the somatic currents.

Since we observed a large variability in the Vm, we speculated that averaging across many events could potentially conceal important differences between iAPs and CSBs. Therefore, we calculated the total magnitude of each current type in the soma for each event in the 8 ms period before iAPs or the first AP of CSBs (Fig. 7C). We found a large variability in the currents underlying both iAPs and CSBs with the distributions entirely overlapping between the two types of events. We got similar results when analysing the origin of the axial currents in the soma (Fig. 7D). This indicates that it is not possible to distinguish CSBs and iAPs before the first AP from the somatic state of the neuron, and suggests that the soma can not control burst firing. Consequently, the somatic current dynamics before the iAP and the CSB presented in Fig. 5Cc-Dd can be regarded as illustrative samples from a broad distribution, but the differences observed between them are not representative.

Next, we analyzed currents in the apical dendrites from the distal trunk region and from the apical tuft. Although we found some small, but significant alterations in the current types in both the trunk (not shown) and the tuft (Fig. 7E), the largest differences were in the origin of the currents driving these regions (Fig. 7F): before CSBs the tuft did not receive inward (excitatory) currents from proximal regions but was driven solely by local excitatory intrinsic and synaptic currents. In contrast, outward currents from the tuft propagated towards the trunk and obliques significantly more during CSBs than during iAPs. However, we still observed a substantial variability between the events indicating that both iAPs and CSBs could be highly diverse. We were wondering whether this diversity could be captured by a few dominant factors along which iAPs and CSBs were segregated.

In order to test this idea, we applied factor analysis to the dataset containing the magnitude of 42 current types in the 3 different dendritic domains (soma, trunk, tuft; see Methods) before the first spike of the event. The factor analysis revealed that the data indeed was low-dimensional: The first two factors together explained almost 80% of the total variance with additional factors providing negligible contribution (Fig. 8A). When we projected the data into the space defined by the first two factors, the datapoints corresponding to CSBs and iAPs tended to occupy different regions of the state space (Fig. 8B) indicating that these factors capture characteristic differences between these event types.

Next, we checked how different current types contributed to these first two factors. We found that the outward currents (GABA and K^{+}) in the tuft region had the largest positive loadings, while the distal inward currents (NMDA and Ca^{2+} currents) had the largest negative loadings to the first factor (Fig. 8C; note that inward currents are negative). Thus, strong excitatory or inhibitory tuft inputs both increase the first factor. We thus interpreted the first factor as capturing the strength of the inputs to the tuft region. Similarly, the second factor had the strongest positive loadings on inhibitory, and negative weights on excitatory currents in the trunk region (Fig. 8C). Interestingly, proximal NMDA and Ca^{2+}-current had opposite effects (Fig. 8C): somatic Ca^{2+}-current, originating from the apical dendrites, increased both factors, while somatic NMDA currents, indicating dominant excitation from basal branches, decreased them. We interpret the second factor as capturing the strength of inputs to the oblique/trunk region of the cell.

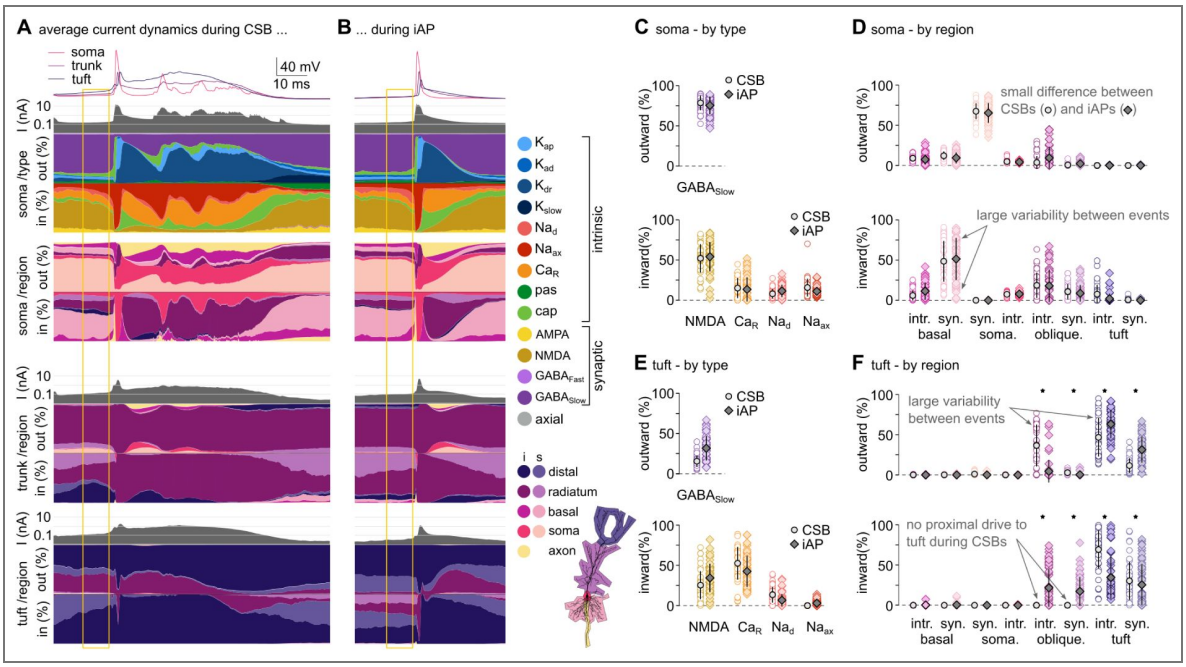

Fig. 7. Currents underlying CSBs and isolated spikes.

A) Average currentscape of CSBs, aligned to the first spike of the bursts (n=41 events). Top: average Vm in the soma, the trunk (d=260 μm from soma) and in a tuft branch (d=470 μm). Second row: Somatic total current and currentscapes by current type and current region. Third row: Total current and currentscape by current region in the trunk. Last row: Total current and currentscape by current region in the tuft. Yellow rectangle before the first spike indicates the region used for the analysis in C-F. **B**) Same as A for isolated spikes (n=58 events). **C**) Contribution of selected membrane current types to outward (top) or inward (bottom) somatic currents in individual CSBs (circles) or APs (dark diamonds). **D**) Contribution of different dendritic regions to the somatic currents in individual CSBs (circles) or APs (dark diamonds). **E-F**) Similar to C-D, calculated for a tuft dendrite.

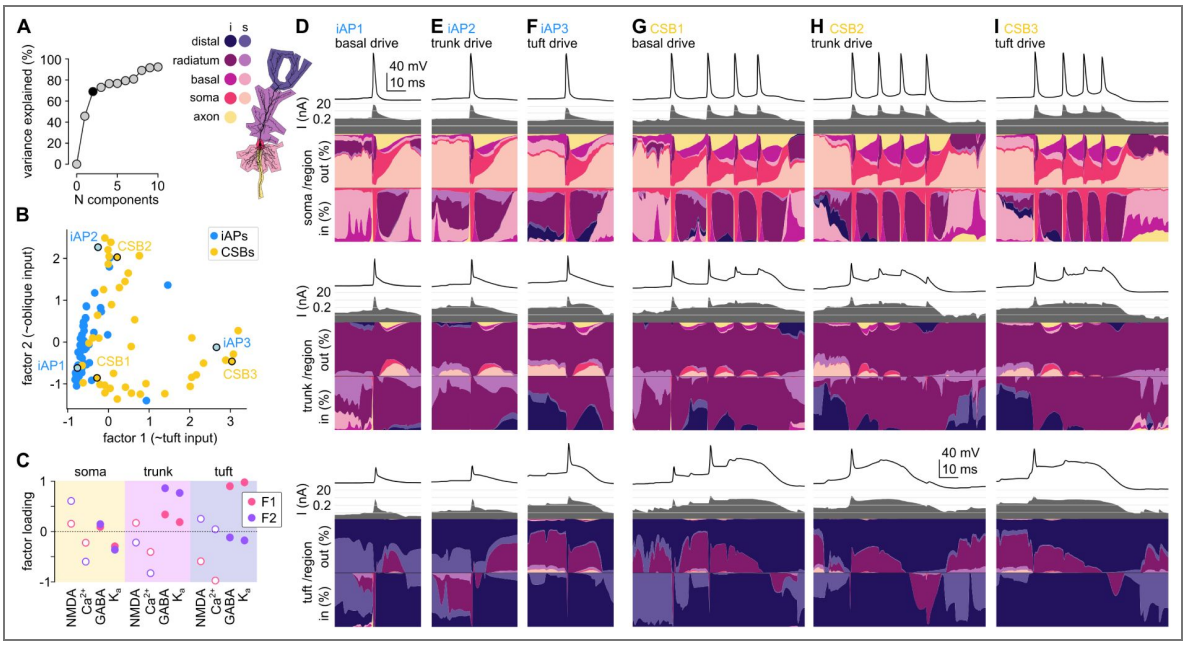

Fig. 8. Structured diversity of the currents preceding CSBs and iAPs.

A) Variance explained as a function of the number of components (factors) considered to reconstruct the magnitude of different current types preceding somatic events (CSBs or iAPs). **B**) Linear projection of the currents to the 2 factors explaining most of the co-variability across somatic events. The six events highlighted with black outline are shown in D-I. **C**) Factor loadings (weights) associated with representative inward (open circles) and outward (filled circles) currents of the two factors (F1: factor 1, pink; F2: factor 2, levander) shown in panel B. **D-I**) Example currentscapes of CSBs (D-F) and iAPs (G-I) with different initiation dynamics.

This analysis revealed that most of the variability between iAPs is confined to a single dimension with low tuft input and a varying degree of oblique or basal excitation (Fig. 8B,D-E). Moreover, iAPs occur only exceptionally at high tuft input levels (Fig. 8F). In contrast, CSBs occupy a greater fraction of the state space with varying tuft and trunk input, but generally avoiding the lowest levels of tuft excitation (Fig. 8B, G-I). Note that occasionally highly similar currents preceded iAPs and CSBs and which of these occurred could depend on later synaptic inputs or subtle differences in the state of intrinsic conductances (Fig. 8B, D-I; see also Fig. S4).

To further elucidate the role of the inputs targeting different dendritic domains in evoking spikes or CSBs, we selectively decreased the input rates at basal, oblique or tuft branches, simulating optogenetic inhibition experiments (Bittner et al., 2015). Specifically, we randomly selected 300 input synapses targeting either of these domains, decreased their input rates by 75%, and measured the changes in postsynaptic spiking and CSB firing. We found that decreasing the tuft input had the strongest effect in reducing both the CSBs and the spike rate of the cell (Fig. S5A). This effect was not explained by the more clustered location of the inhibited synapses in the tuft (Fig. S5A), further emphasizing the crucial role of the tuft in controlling the excitability of the cell. In agreement with the experimental results (Bittner et al., 2015), the tuft inhibition caused a larger reduction in the CSBs rates (≈ 20% of the control) than in the spike rates (≈ 35% of the control; Fig. S5). Nevertheless, inhibition of basal or oblique synapses also decreased the number of CSBs, which confirms that complex spike bursts are not exclusively triggered by distal inputs in our model.

Taken together, these analyses demonstrated that, in agreement with previous experimental results (Takahashi and Magee, 2009; Bittner et al., 2015; Grienberger and Magee, 2022; Park et al., 2025) strong distal inputs facilitate the generation of CSBs. However, in our model there was no need for exceptionally high input synchrony at the tuft synapses neither for Ca^{2+}-hotspots in the dendrites to evoke CSBs. Instead, CSBs could be evoked under a large variety of synaptic and intrinsic current conditions by input to apical dendrites even at relatively weaker tuft excitation.

Discussion

Summary

In this paper, we first introduced the extended currentscape technique to quantify and visualize the effect of dendritic events on the somatic response of a biophysical model neuron. Next, we illustrated the extended currentscape method in standard simulation experiments probing dendritic integration. Our method could compactly and intuitively capture the sequence of dendritic events leading somatic APs in models with simple morphology or to a superlinear somatic response in models with realistic dendritic arbor. After validating the model using spatiotemporally restricted stimuli, we turned towards *in vivo*-like inputs and examined dendritic activity during simulated place field dynamics. We found that although correlated activity dominated the dendritic Vm dynamics of the model, the extended currentscape method could identify various dendritic events underlying somatic spikelets, action potentials, and complex spike bursts.

Next, we contrasted the somatic and dendritic current dynamics preceding iAPs and CSBs. Although we found a large diversity of current contributions before the two event types, the distributions of the currents were surprisingly similar before CSBs and iAPs. Finally, we applied factor analysis to the somatic and dendritic currents and showed that the large variability is dominated by two factors, corresponding to inputs to the distal and proximal apical dendrites. We found that CSBs and iAPs could occur at variable oblique and basal input levels, but strong apical inputs facilitated the generation of CSBs.

The extended currentscape

Our analysis is based on the extended currentscape method to identify the type and origin of membrane currents that drive the activity in any segment of a neuron with spatially extended morphology. Our technique relies on simulating the neuron using a standard biophysical modeling

software (Hines and Carnevale, 1997) and measuring the membrane currents and the membrane potential in each model segment at every timestep. We used Kirchhoff's current law to partition the axial currents between neighboring pairs of segments proportionally to the composition of the in-coming or the outgoing membrane currents, depending on the direction of the axial current. We applied this partitioning algorithm iteratively starting from the tip of the dendrites (leaf nodes) and proceeding towards the target segment.

In this paper, we partitioned the axial currents either by the channel type or by the dendritic region of the associated membrane currents. Partitioning the axial currents by the type of the membrane currents generating them provides a compact and intuitive summary of the sequence of events mediated by different intrinsic and synaptic conductances during various neuronal activity patterns, illustrated here for the case of theta activity, spiking and bursting in place cells. In contrast, partitioning the axial currents by their dendritic origin reveals the relative contribution of the different dendritic domains to driving the neural response at any given time. Here we distinguished only a few major regions (axon, soma, basal, oblique and tuft dendrites) within the cell, but different divisions, with more fine grain compartmentalization or alternative combinations with partitioning by current type, would be an interesting future application of the method.

Previous approaches dissecting the contribution of individual ion channel types to the somatic response of a cell relied on targeted perturbation of the available biophysical mechanisms both in real neurons (Wei et al., 2001; Ariav et al., 2003; Losonczy and Magee, 2006; Smith et al., 2013; Palmer et al., 2014) and in biophysical models (Gasparini et al., 2004; Gómez González et al., 2011; Hay et al., 2011; Behabadi et al., 2012; Grienberger et al., 2014; Goetz et al., 2021; Kim et al., 2023). However, interpreting the result of these perturbations is hampered by the potential interactions between various biophysical mechanisms, especially under *in vivo* conditions (Smith et al., 2013; Palmer et al., 2014). For example, Losonczy and Magee (2006) found that blocking dendritic Na^+-spikes inhibited both the fast and the slow components of the superlinear somatic response. They posited that the supralinear input-output function critically depends on the facilitation of NMDA spikes by local dendritic Na^+spikes. Conversely, Smith et al. (2013) found the blocking NMDA receptors greatly reduced the number of local dendritic fast spikes in layer 2/3 PNs, suggesting a reciprocal interaction between NMDA– and Na^+–spikes. Here we propose an alternative approach that does not require perturbations but calculates the contribution of ion channel types directly from the recorded axial and membrane currents, albeit currently only in biophysical models. Importantly, our method works equally well under a wide variety of input conditions, including stimulation localised to a single dendritic branch or distributed throughout the entire dendritic tree.

Biophysical model

Our biophysical model CA1 neuron is a modified version of the model of Jarsky et al. (2005) originally developed to capture the generation and propagation of Na^+ spikes along the apical trunk and later modified to account for the integration of synaptic inputs via Na^+-, and NMDA-spikes in basal and oblique dendrites (Losonczy and Magee, 2006; Ujfalussy and Makara, 2020). As Ca^{2+}-spikes in CA1 PNs are primarily mediated by R-type channels (Takahashi and Magee, 2009), we added Ca^{2+}channels using kinetic scheme taken from (Magee and Johnston, 1995) to model dendritic Ca^{2+}spikes. Our model was able to generate complex spike bursts, with associated dendritic plateau potentials upon current injection or synaptic stimulation into the dendrites. However, this model is not yet able to capture all, potentially important, properties of Ca^{2+}-spikes in CA1 neurons, including their failure to generate Ca^{2+}-spike upon strong somatic current injection in most cells, the delayed initiation of the Ca^{2+}spikes, the inhibitory effects of the Na^+-APs on Ca^{2+} spike initiation (Golding et al., 1999) and the generation of prolonged somatic plateau potentials (Bittner et al., 2015). Currently we are not aware of any CA1 PN model that would be able to reproduce these experimental observations (see the references in Sáray et al. 2021) indicating the need for further research revealing the exact biophysical mechanisms of dendritic Ca^{2+}spikes.

The membrane potential response of the model to *in vivo*-like synaptic inputs was dominated by a low-dimensional, global dynamics (Fig. 4C-E). The shape and the variance explained by the first two principal components of Vm covariance matrix was very similar to the data reported in a recent *in vivo* voltage imaging study (Lee et al., 2026), indicating that back-propagation of APs is the most prominent event organising dendritic activity. However, our model also exhibited a lot of local dendritic events each restricted to only a few branches (Fig. 4H-J). Importantly, in our model localised dendritic events occurred primarily in distal, terminal branches that are more likely to be omitted during single-cell voltage imaging studies (Lee et al., 2026). In our model the proximal dendrites were highly synchronized with the soma, whereas previous Ca^{2+}-imaging studies reported some level of uncoupling of somatic and dendritic activity (Sheffield and Dombeck, 2015; Sheffield et al., 2017; Rolotti et al., 2022). This may be explained by the unreliability of Ca signal measurements to report Vm changes (Tran-Van-Minh et al., 2016; Weber et al., 2016; Landau et al., 2022). Our analysis also indicates that global events may dominate the PCA analysis (Lee et al., 2026) even when local dendritic regenerative events are widespread, and the neuron is mainly driven by strong, functionally clustered synaptic inputs to a few dendritic branches (Ujfalussy and Makara, 2020).

We used identical biophysical properties and input statistics for the tuft and distal oblique branches in our model. Although numerous differences are known regarding both the inputs (Witter et al., 1989; Isomura et al., 2006; Milstein et al., 2015) and dendritic physiology (Nicholson et al., 2006; Bittner et al., 2012), many of the relevant parameters are still underconstrained. We wanted to avoid overfitting by keeping the model relatively simple (Herz et al., 2006). Moreover, by maintaining identical inputs and ion channel distribution we could distinctly highlight the special role of tuft morphology in CSB generation and altering the inputs or the ion channel density for the tuft would make these interpretation of the results more ambiguous. Elucidating the specific role of the regional differences in inputs or their local processing in CSB generation could be the subject of future investigations.

Implications for burst firing

While acknowledging the incompleteness of our biophysical model, we believe that our simulations still provide several important insights into the generation of Ca^{2+}-spikes under *in vivo*-like conditions. First, it was unclear whether increased Ca^{2+}-channel density in the tuft region or special perforant path input patterns are necessary for facilitating burst firing in CA1 PNs (Bittner et al., 2015; Grienberger and Magee, 2022). Our simulations demonstrated that distal tuft branches are especially well suited to promote burst firing even with uniform Ca^{2+}channel density and similar input statistics along the apical subtree. This observation suggests that it is the morphology of the cell and the presence of strong inhibitory conductance load on the apical trunk that makes tuft branches more excitable than oblique dendrites.

Second, we observed a high variability between the activation of individual tuft and oblique branches during CSB firing. This observation is reminiscent of Ca^{2+} imaging data from the distal dendrites showing a variable recruitment of tuft branches during place field formation and subsequent traversals (O'Hare et al., 2025). Our simulations clarified that tuft Ca^{2+}-plateaus are not necessarily associated with uniform tuft activation and the high variability between branches can be caused by diversity in the synaptic inputs they receive.

Third, we found a large heterogeneity among the input currents preceding CSBs: while some CSBs were elicited at high tuft currents, many were triggered at lower or intermediate level of distal inputs. This suggests that the presence of distal inputs facilitates rather than controls the emergence of CSBs. This finding explains why it is possible to elicit plateau potentials *in vivo* using somatic current injection during BTSP (Behavioral Time Scale Plasticity) induction (Bittner et al., 2015) where the same stimulus usually fails to evoke Ca^{2+}-spikes *in vitro* (Golding et al., 1999) and predicts that reduction of CA3 inputs to the oblique or basal dendrites would also decrease CSB rate, BTSP induction and the associated reward zone over-representation similarly to the effect of inhibiting the more distal EC inputs (Fig. S5; Bittner et al. 2015; Grienberger and Magee 2022; Fan et al. 2023). The facilitatory action of distal tuft inputs on CSBs is

reminiscent of the conjunctive bursting mode, where bursts are generated by a synergistic interaction between different input streams (Larkum et al., 1999; Naud and Sprekeler, 2018; Takahashi and Magee, 2009) and is consistent with the conclusions of the recent study postulating that dendritic plateaus are initiated within the distal regions of stratum radiatum by strong inputs to both distal tuft and radial oblique dendrites (O'Hare et al., 2025). The ability of CA3 inputs to the radial oblique dendrites to influence CSB generation and BTSP induction could be an important cellular mechanism to enable generalization across consecutive experiences (Vaidya et al., 2025; Qian et al., 2025).

Although we could frequently observe complex spike bursts in our simulations, we did not observe large amplitude (>20 mV) prolonged (> 100 ms), plateau-like depolarization events in the soma with substantially reduced AP amplitude (Bittner et al., 2015) during naturalistic synaptic inputs. However, a response more similar to plateau potentials could be evoked in our model by combining *in vivo*-like synaptic stimulation with direct somatic current injection (Fig. S1E). We thus speculate that the generation of plateau potentials might require strong perisomatic excitatory currents. Our preliminary simulations suggest that Ca^{2+}-channels added to the basal dendrites can provide this additional excitation. The bio-physical mechanism and the natural synaptic input conditions that lead to CSB versus plateau potentials in CA1 pyramidal neurons is a promising subject for future research.

Limitations of the study

In order to make the partitioning algorithm self-consistent, we had to also include the capacitive current among the membrane currents in Eq. (1): It is possible that in a given segment the only inward current may be the capacitive current but the axial current is still outward. The capacitive current acts as a delay line in the membrane equation, representing the indirect effect of currents that were active earlier and had charged the membrane capacitance. In practice, we found that the capacitive current may sometimes have a large contribution to the membrane dynamics (Fig. 5Ce) and can thus mask the delayed contribution of various membrane currents. A potential extension of our method would be to also partition the capacitive current, but it is not clear how this could be achieved self-consistently and is beyond the scope of our current paper.

Our partitioning algorithm identifies only the direct contribution of the membrane currents to membrane potential changes in the target compartments, and ignores all indirect effects. This property follows from the presumption that there must be a direct chain of links between cause and effect (Pearl, 2009), in particular, there must be a continuous flow of axial current between the membrane current in a distal dendrite and the change it triggers in the target. Thus, our method is blind to indirect effects otherwise known to be present in complex dendritic trees, such as certain types of off-the-path inhibition (Gidon and Segev 2012; but see also Fig. 2P). Revealing the contribution of such indirect causes under complex synaptic stimulation would require causal perturbation methods that have been proposed earlier in the context of synaptic effects (Bicknell and Häusser, 2021).

Testing the model: electrophysiology or voltage imaging

Experimental testing of the partitioning algorithm presents considerable challenges. Accurate measurements of the contribution of membrane current types to the somatic activity of a neuron require simultaneous measurement of all membrane currents and potentials, which is not feasible with current experimental methods.

Although measuring individual current contributions is not feasible in real neurons, a recent study performed whole-cell recordings in visual cortical neurons *in vivo* and used the systematic change of the input resistance with depolarization to estimate the contribution of intrinsic and synaptic currents to neuronal responses (Li et al., 2020). They found that during visual stimulation the intrinsic and synaptic conductances have comparable contribution to the subthreshold membrane potential changes of the cell, with intrinsic channels amplifying the synaptic response. Similar analysis on *in vivo* hippocampal recordings could test whether synaptic and intrinsic conductances amplify or counteract each other *in vivo* (Hoffman et al., 1997;

Bittner et al., 2015; Epsztein et al., 2011; Cohen et al., 2017; Valero et al., 2022). However, in the absence of dendritic recordings, this study was unable to identify the spatial origin of synaptic and intrinsic changes within the dendritic tree.

More direct test of current propagation in real neurons would require measuring the membrane and axial currents at multiple spatial locations. As a recent step towards achieving this Meszéna et al. (2023) combined somatic patch-clamp recordings and multichannel extracellular recordings to reconstruct the spatiotemporal distribution of the membrane currents and the membrane potential of a single neuron during AP generation. Alternatively, one could use *in vivo* voltage imaging to monitor the membrane potential of dendrites and the soma simultaneously (Abdelfattah et al., 2023; Liao et al., 2024; Park et al., 2025; Lee et al., 2026). From the local membrane potential one can calculate the axial currents after estimating the intracellular resistivity and the dendritic cable diameters. Our method of partitioning the axial current by its origin within the dendritic tree can be applied directly to this kind of data. Therefore, such data could be used to directly test both the behaviour of the biophysical model under *in vivo*-like input conditions (Fig. 4F-G) and the diversity in the origin of the input currents before single spikes and CSBs in CA1 neurons (Fig. 8).

Methods

Biophysical models

All simulations were performed with the NEURON simulation environment (version 8.2) embedded in Python (version 3.9 and 3.11). Code for simulating the biophysical model, preprocessing, axial currentscape calculation and visualization are available at *https://github.com/bencefogel/currentscapes-invivo-demo*. Code for simulating the simplified model is available at *https://github.com/bencefogel/currentscapes-simple-model-examples*.

Simplified neuron model (Fig. 2)

A simplified model was constructed using a minimal morphology consisting of a soma and three dendritic sections. The soma was connected to a primary dendrite (dend1), which bifurcated into two secondary dendrites (dend2 and dend3). All sections were modeled as unbranched cylinders.

The soma had a diameter and length of 20 μm. The primary dendrite (dend1) was 100 μm long with a diameter of 2 μm and was discretized into 11 segments to ensure adequate spatial resolution. The two secondary dendrites (dend2 and dend3) each had a length of 50 μm and a diameter of 1.5 μm, with 5 segments per branch. Dend2 and dend3 were attached to the distal end of dend1, forming a simple three-branch dendritic arbor.

Specific membrane capacitance was set to 1 μF/cm^2. Passive leak conductance was implemented using NEURON's pas mechanism, with a uniform leak reversal potential of -66 mV. The soma had a reduced leak conductance (1/40000 S/cm^2), whereas dendritic sections used a leak conductance of 1/20000 S/cm^2. Axial resistivity (Ra) was set to 100 Ωcm for the soma and 800 Ωcm for all dendritic compartments.

Active voltage-gated currents were included in the soma and dendrites to support basic excitability. The kinetic parameters of the active conductances were identical to those in the morphologically detailed model (see below; Fig. S6). The soma contained fast sodium and delayed-rectifier potassium channels with maximal conductances of g_{Na} = 0.02 S/cm^2 and g_K = 0.002 S/cm^2, respectively. All den-dritic compartments expressed lower-density dendritic sodium and delayed-rectifier potassium currents with $g_{Na,dend}$ = 0.007 S/cm^2 and $g_{K,dend}$ = 0.0002 S/cm^2, providing modest active boosting and limited back-propagation. Synaptic mechanisms included AMPA and GABA$_{fast}$ receptors implemented using Exp2Syn. AMPA synapses used τ_1 = 0.1 ms and τ_2 = 1 ms with a reversal potential E_{AMPA} = 0 mV, while GABA$_{fast}$ synapses used τ_1 = 0.1 ms, τ_2 = 4 ms, and E_{GABA} = −65 mV with a synaptic conductance g_{GABA} = 10 nS. Excitatory synaptic strengths varied by experiment: AMPA conductance was set to 0.5 nS for Fig. 2A-C and O, and 2.5 nS for Fig. 2N and P.

Synaptic inputs were generated using NetStim objects in NEURON to produce brief, high-frequency bursts of presynaptic events. Each stimulus (for both AMPA and GABA) consisted of five spikes delivered at 0.1 ms intervals, corresponding to a set of synchronous presynaptic spikes designed to evoke localized dendritic responses.

CA1 neuron model

We used a modified version of a previously developed CA1 PN model (Jarsky et al., 2005; Ujfalussy and Makara, 2020), maintaining the same ion channel distributions and densities for Na^+, K^+ and proximal and distal type K^+ channels as described in Ujfalussy and Makara (2020) (Fig. S6).

To capture dendritic Ca^{2+} spikes and somatic CSBs, we added an R-type Ca^{2+} channel to the model. The Ca^{2+} channel kinetics were based on the steady-state activation and inactivation curves fitted by Magee and Johnston (1995), with a slight modification to allow for a larger window current (Fig. S1A). The Ca^{2+} channel was expressed in the apical dendritic tree with a uniform distribution and an ion channel density of 0.006 S/cm^2.

Furthermore, we added a high-voltage activated, slow K^+ channel that was used to simulate the combined effect of multiple K^+ channels including Ca^{2+}-activated K^+ channels, contributing to the repolarization after the Ca^{2+} spikes. The slow K^+ channel was expressed in the apical dendritic tree with a uniform distribution and an ion channel density of 0.001 S/cm^2.

The idealized CA1 place cell received inputs from 2000 excitatory and 200 inhibitory presynaptic neurons. We simulate the activity of excitatory and inhibitory neurons during the movement of a mouse on a 2-m long circular track with constant velocity of 20 cm/s. Each presynaptic excitatory neuron had a single idealised place field and represented the CA3 inputs received by the postsynaptic CA1 neuron.

Reliable place cell tuning can be achieved by functional synaptic clustering without increased excitatory drive in the place field (Ujfalussy and Makara, 2020) or via strong excitatory drive without input clustering (Grienberger et al., 2017; Ujfalussy and Makara, 2020). However, experimental data indicates that both of these mechanisms are present and contribute to the activity of place cells (Adoff et al., 2021; Tasciotti et al., 2025). Excitatory synapses were placed randomly with a uniform distribution on the entire dendritic tree, except 240 inputs, active in the postsynaptic place field in middle of the track, that were selected to form functional synaptic clusters. There were a total of 12 clusters, and each cluster had 20 synapses. Synaptic clusters were placed on the middle of terminal dendritic branches longer than 60 μm with 1 μm distance between the synapses. This relatively strong clustering favoured the generation of local dendritic spikes (Ujfalussy and Makara, 2020).

Although interneurons can display spatial tuning, they typically have a broad tuning with low selec-tivity (Ego-Stengel and Wilson, 2007; Dupret et al., 2013; Geiller et al., 2020). Albeit weak disinhibition within the place field can contribute to the selective firing of place cells (Geiller et al., 2022; Valero et al., 2022), this was not necessary for place cell activity in novel environments (Geiller et al., 2022) and the overall inhibitory input to place cells is largely untuned (Grienberger et al., 2017). Inhibitory presynaptic inputs were modulated by theta oscillation (Csicsvári et al., 1999) but were not spatially tuned (Wilson and McNaughton, 1994; Dupret et al., 2013). The inhibitory synapses were divided into two groups with 80 synapses targeting the soma and the apical trunk and the remaining synapses distributed randomly along the entire dendritic tree (Megias et al., 2001).

The model included AMPA and NMDA excitation and slow and fast GABA inhibition. Synaptic parameters were kept identical to those described in Ujfalussy and Makara (2020) (see Fig. S7 for kinetic parameters). To induce reliable firing within the neuron's place field, we increased the AMPA (from g_{max} = 0.6 nS to g_{max} = 1 nS) and NMDA (from g_{max} = 0.8 nS to g_{max} = 1.2 nS) conductance associated with the clustered synaptic inputs, consistent with the primary role of synaptic plasticity in place field formation (Bittner et al., 2015; Adoff et al., 2021; Heredi et al., 2025). Inhibitory synapses (both slow and fast) had a maximal conductance of g_{max} = 0.2 nS.

Simulation of the model

We simulated place cell activity for 10 seconds as the hypothetical animal completed a single lap on the track. A total of 16 simulations were run, each with different random configurations of synapse placement and presynaptic input patterns.

In the NEURON software, neurons are modelled as a series of sections, which represent unbranched parts of continuous cable, such as dendrites or axon. These sections are connected together to form an acyclic graph, according to the morphology of the neuron. Each section is divided into multiple segments of equal length.

NEURON uses a normalized distance to express locations along a section, where 0 represents the start (closest to the parent section) and 1 represents the distal end. To compute membrane dynamics, NEU-RON calculates membrane potentials and membrane currents at discrete positions, known as internal nodes, located at the center of the segments. The accuracy of the partitioning, like the accuracy of the numerical simulation of spatially extended cables, can be increased by choosing finer discretization, ie., larger number of segments. During our simulations, the number of segments within each section was chosen to ensure accurate description of signal propagation within the cable with reasonable computational efficiency. As a rule of thumb, we found that axial current partitioning is accurate if the proportion of the magnitude of the membrane currents and the magnitude of the axial current was small. This proportion was on average ≈ 1 : 17 for non-terminal branches in our case.

In addition to the internal nodes, located at the center of the segments, there are external nodes located at the 0 and 1 ends of each section. These external nodes are only used to connect segments, but no membrane mechanisms (synapses or ion channels) are associated with these external nodes.

During each simulation, we recorded the membrane potential (mV), intrinsic (mA/cm^2) and synaptic currents (nA) of all segments of the neuron (N_{sec} = 161 sections and N_{seg} = 1529 segments in total, including the $2N_{sec}$ internal segments; see below). This was the raw dataset we used to calculate the currentscapes. We also saved the model connectivity structure between segments together with the axial resistance values (MΩ) to calculate axial currents offline. Finally, we measured the area (μm^2) of each segment, which is needed during the preprocessing of membrane currents.

During the simulation, state variables were computed using NEURON's built-in multi order variable time-step integration method. For subsequent preprocessing and currentscape calculation, the recorded output vectors were downsampled to 5 kHz.

Preprocessing

The goal of preprocessing was to convert the raw dataset, saved by NEURON into two tables that we can use to calculate the partitioning of the axial currents. The first table contains the membrane currents for each segment and for each time step. The second table contains the axial currents between the segment pairs.

Preprocessing membrane and synaptic currents

The preprocessing starts with choosing a target section for partitioning. The extended currentscape will partition the axial currents flowing into this target section. If we want to partition the axial currents flowing into different sections (e.g., soma and a tuft compartment), we have to repeat the pruning (see below) and the partitioning steps with the novel target.

All segments that belong to the target section were merged for further analysis (that is, the membrane currents of the segments were summed and no axial current was calculated within the target section). The connections between the segments of the target section and its child branches were reassigned to the segment of the merged target.

Each synapse is represented by a conductance-based mechanism that injects current into the post-synaptic compartment when triggered via a NetCon object. Since each NetCon delivers spikes independently, and multiple synapses can target the same segment, synaptic currents (in nA) were summed per segment and per synaptic type (AMPA, NMDA, $GABA_{fast}$, $GABA_{slow}$) to accurately capture the total synaptic input.

To ensure consistency in subsequent calculations, intrinsic currents were converted from units of mA/cm^2 to nA. This was done by multiplying the recorded current by the corresponding segment area (in μm^2) and applying a scaling factor of 10^{-2}. Finally, intrinsic and synaptic currents were combined into a single data structure, where each row corresponds to a unique segment and current type pair, and each column is a simulation time point.

The core algorithm underlying the extended currentscape calculation is the axial current partitioning algorithm (see below). By default, this algorithm decomposes the axial current of a target compartment into underlying membrane current components. However, alternative variants of the partitioning algorithm can be applied if the membrane current data structure is reindexed and recalculated. In region-specific partitioning, membrane currents are reassigned based on their location within different subcellular regions (for example, axon or dendrite). These different approaches can also be combined in a flexible way to measure e.g., the somatic influence of NMDA channels in a particular dendritic branch. In this study, we demonstrate two such variants: Membrane current type-specific partitioning and a combined partitioning where we distinguished 5 subcellular regions (axon, soma, basal dendrites, trunk+oblique dendrites and tuft dendrites) and 2 current types (synaptic and intrinsic currents). The intrinsic category incorporated all non-synaptic currents, including capacitive and passive currents.

Preprocessing axial currents

To compute axial currents we first created a list with the adjacent segment pairs between which axial currents will be calculated. Connections between sections (branches) are implemented in NEURON through a pair of external nodes: one at the distal end of the parent section and another at the proximal end of the child section. Although these nodes formally belong to different sections (parent and child), they have identical membrane potential as they represent the same point within the cable, so we merged them to remove the duplicates from our primary dataset.

The axial current between a parent and child segment is computed using Ohm's law:

$$I_{\text{ax}} = \frac{V_{\text{parent}} - V_{\text{child}}}{R_i} \tag{2}$$

Here V_{parent} and V_{child} denote the membrane potentials of the parent and child segments, respectively, and $R_i$denotes the axial resistance between them.

Extended Currentscape Calculation

The extended currentscape calculation requires the following inputs: the preprocessed membrane and axial currents across all segments, a specified target segment, and a defined partitioning strategy, such as current type-specific or region-specific partitioning.

The first step in calculating the extended currentscape was to separate positive and negative membrane currents. Certain currents, such as capacitive currents, can be both inward and outward at the same time in different compartments. Without separation, such positive and negative currents would partially cancel each other out, reducing the contribution of the current type during the extended currentscape calculation. This effect is even more pronounced when partitioning the axial currents by the origin (see below): Strong positive and negative currents from two different basal branches can cancel each other, largely concealing their overall contribution to the somatic activity. By treating the positive and negative membrane currents independently, we ensured that the outward and inward membrane current components of the target's axial current are calculated separately.

Following preprocessing, including reindexing and recalculation of membrane currents when required by the region-specific partitioning, a directed graph was constructed at each time step. The nodes of the graph represent individual neuronal segments and the directed edges indicate the direction of axial currents flowing between them. We create two separate subgraphs starting from the target segment: one for the inwardly flowing and one for the outward axial currents. Partitioning is calculated independently for the two subgraphs, with the inward (outward) axial graph partitioned according to the inward (outward) membrane currents, respectively.

To determine the partitioning order, we performed a depth-first search (DFS) on the two directed graphs starting from the target segment mowing towards the terminals along each dendritic branch separately. The search proceeds through the directed graph until it encounters collision points, where the axial current reverses its direction. At these points, current propagation is blocked: Distal nodes beyond the the first reversed edge (*collision edge*) are excluded from further calculations, as they do not directly influence the target compartment. In a benchmark simulation this pruning process reduced the size of the tree (which is proportional to the computational cost of the currentscape calculation) by 68% (50–80%). The two subgraphs identified by this search define the structures upon which axial current partitioning is performed.

Partitioning is carried out iteratively, beginning from the leaf nodes of the subgraph and progressing toward the target node. At each time step, the axial current is partitioned into inward (negative) or outward (positive) membrane current components depending on the direction of the axial current flow. Specifically, for a given time point t, the positive or negative membrane currents $I^{\mathrm{m,child}}$ of the child node are first normalised by their sum. The resulting fractions are multiplied by the magnitude of the axial current I^{ax} flowing between the child and the parent nodes. The contribution of membrane current of type i to the axial current can be expressed as:

$$I_i^{\mathrm{part}}(t) = \frac{I_i^{\mathrm{m,\,child}}(t)}{\sum_i I_i^{\mathrm{m,\,child}}(t)} I^{\mathrm{ax}}(t) \tag{3}$$

The partitioned axial current components $I^{\mathrm{part}}(t)$ are then added to the corresponding membrane currents of the parent section according to:

$$I_i^{\mathrm{m,\,par}}(t) = \bar{I}_i^{\mathrm{m,\,par}}(t) + I_i^{\mathrm{part}}(t) \tag{4}$$

where $\bar{I}_i^{\mathrm{m,par}}(t)$ is magnitude of the membrane current type i measured in the parent segment. This procedure is repeated iteratively for each pair of nodes along the subgraph until the target compartment is reached.

The final output of the extended currentscape calculation consists of two data structures, each including the partitioned axial currents of the target compartment: one containing the inward membrane currents and the other containing the outward membrane currents in each time step. Simulating the morphologically detailed CA1PN model and performing the partitioning at 5 kHz temporal resolution on a 1 s long simulation took 75 min. on a MacBook Pro (2019) computer with 2.6 GHz 6-Core Intel Core i7 processor and 16GB memory.

Data Analysis

CSBs and isolated spikes

CSBs were detected by first smoothing the somatic Vm with a 20 ms Gaussian kernel and then detecting the crossing of a -55 mV threshold of the smoothed subthreshold Vm (Fig. 4B). The start of the CSB was defined as the time of the first spike after crossing this threshold. Isolated spikes were defined as action potentials with a distance of at least 30 ms from the closest AP.

Ca^{2+}-spike detection

Dendritic Ca^{2+}-spikes (Fig. 6C-D) were detected by smoothing the dendritic Vm with a 4 ms Gaussian kernel and then detecting the crossing of a -35 mV threshold of the smoothed subthreshold Vm (Bittner et al., 2015).

PCA of dendritic voltage

We recorded the Vm in the middle segment of all dendritic and somatic compartments of the model and calculated the covariance matrix of the z-scored dendritic voltages in each run separately. Fig. 4C shows the average of these 16 covariance matrices. PCA was then performed by calculating the eigenvalues and eigenvectors of the covariance matrices separately (Fig. 4D-E).

Dendritic events

Dendritic Vm peaks were detected in the central segment of each dendritic section by the find_peaks function from the signal modul of the scipy python package with parameters height=-30 mV and prominence=30 mV. Fig. 4F shows the histogram calculated from the time difference between dendritic events in all branches and the closest somatic action potential. We defined the spatial extent of dendritic events as the number of interconnected dendritic branches that each showed a local Vm peak (as defined above) within < 2 ms of the Vm peak in at least one of the neighbouring branches.

Dendritic domains

In Fig. 6A-B we show the average Vm in different dendritic domains during CSBs and isolated APs. We included all terminal branches with $L > 60\ \mu m$ in this analysis (basals: $N_{basal} = 30$, average distance from the soma: $D_{basal} = 135\ \mu m$; obliques: $N_{oblique} = 19$, $D_{oblique} = 313\ \mu m$; $N_{tuft} = 9$, $D_{tuft} = 729\ \mu m$;).

Average currentscapes

To calculate the average currentscapes in Fig. 6 we first calculated the percentage of the different current shares of each event and then averaged the percentages across the events.

Factor analysis

Factor analysis in Fig. 8 was performed using the partitioned somatic, trunk, and tuft current types before the first spike of the CSB or iAP events. Specifically, we averaged the magnitude of the incoming current types in the interval $t = \{-10, -2\}$ before each event. We performed the averaging separately for the positive and negative currents for all types with nonzero variance (e.g., NMDA currents are always inward, so their contribution to outward currents has zero mean and variance). For this analysis, we used the raw current magnitudes instead of the percentages. We performed factor analysis using the FactorAnalysis function using sklearn's decomposition module.

Simulating optogenetic inhibition

We simulated targeted optogenetic inhibition of different dendritic domains (Fig. S5) by randomly selecting a similar number ($E[n] = 300$) of presynaptic inputs and decreasing their firing rate to 25% of their baseline value. In different experiments, we selected inputs targeting either basal, oblique, or tuft dendrites.

Supplemental Figures

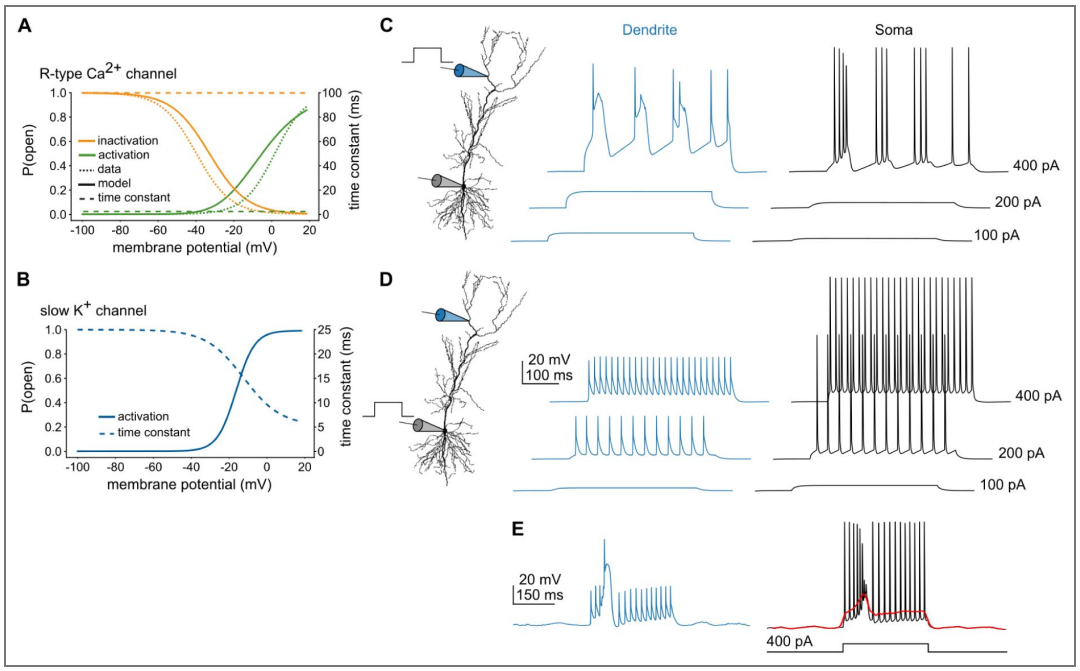

Fig. S1. Biophysical model of burst firing in CA1 PNs. A) Steady-state activation and inactivation curves (left axis, solid lines) and the time constants (right axis, dotted) of the R-type Ca^{2+}channel used in the model. Dotted lines illustrate sigmoid curves fitted to data in Magee and Johnston (1995). **B**) Steady-state activation curve (left axis, solid) and time constant (right axis, dashed) of a slowly activating K^+ channel. **C-D**) Dendritic (blue) and somatic (black) Vm response of the model to dendritic (C) and somatic (D) current injections. The model has a lower current-threshold for Na^+-spikes in the soma and for Ca^{2+}-spikes in the dendrites. Note, that CSBs can be triggered by stronger somatic current steps in the model (not shown). For similar experimental data see Golding et al. (1999). **E**: Dendritic and somatic Vm responses of the model to a 300 ms, 400 pA somatic current injection under in vivo-like synaptic input conditions (during theta activity, outside the place field, as in Fig. 5B). The red line indicates the smoothed somatic Vm. Under these conditions, a dendritic Ca^{2+}-spike and an associated somatic CSB can be evoked by somatic current injection. For similar experimental data see Bittner et al. (2015).

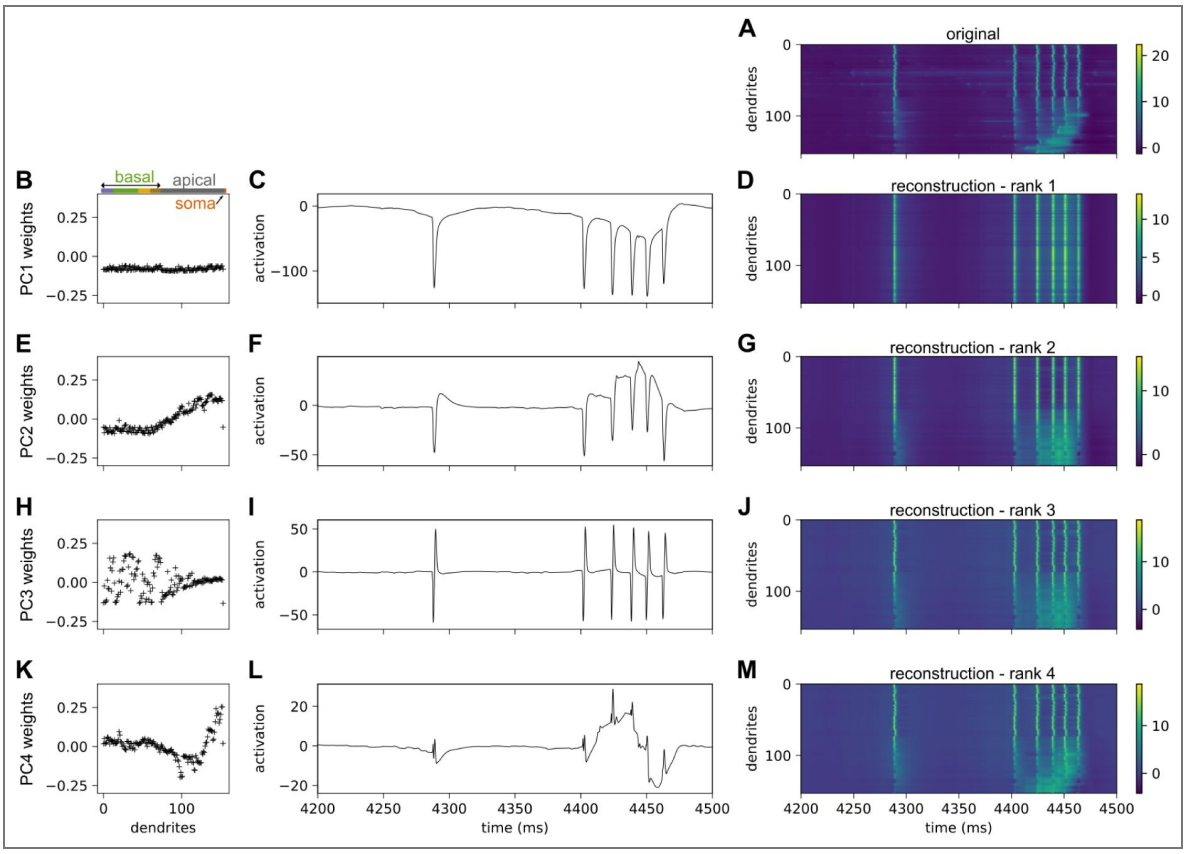

Fig. S2. Dynamics of dendritic Vm PCA components.

A) Short segment of the z-scored Vm of the dendritic branches (rows; soma is the last) of the simulated neuron during *in vivo*-like synaptic stimulation. The cell fired an action potential around t = 4300 ms and a CSB around t = 4400. Dendrites are ordered by morphology as in Fig. 4E. **B)** The weights of the first component (PC1) in an example simulation. Dendritic branches are ordered as in Fig. 4E. **C)** The temporal activation dynamics of the first component (PC1) in an example simulation on the same segment shown in A. **D**) Reconstruction of the dendritic membrane potentials using the first PCA components. **E-M** Similar to A-C for the second (E-G), third (H-J) and fourth (K-M) PCA components. The reconstructions in panels G, J and M used all components up to the given rank. Related to Fig. 4

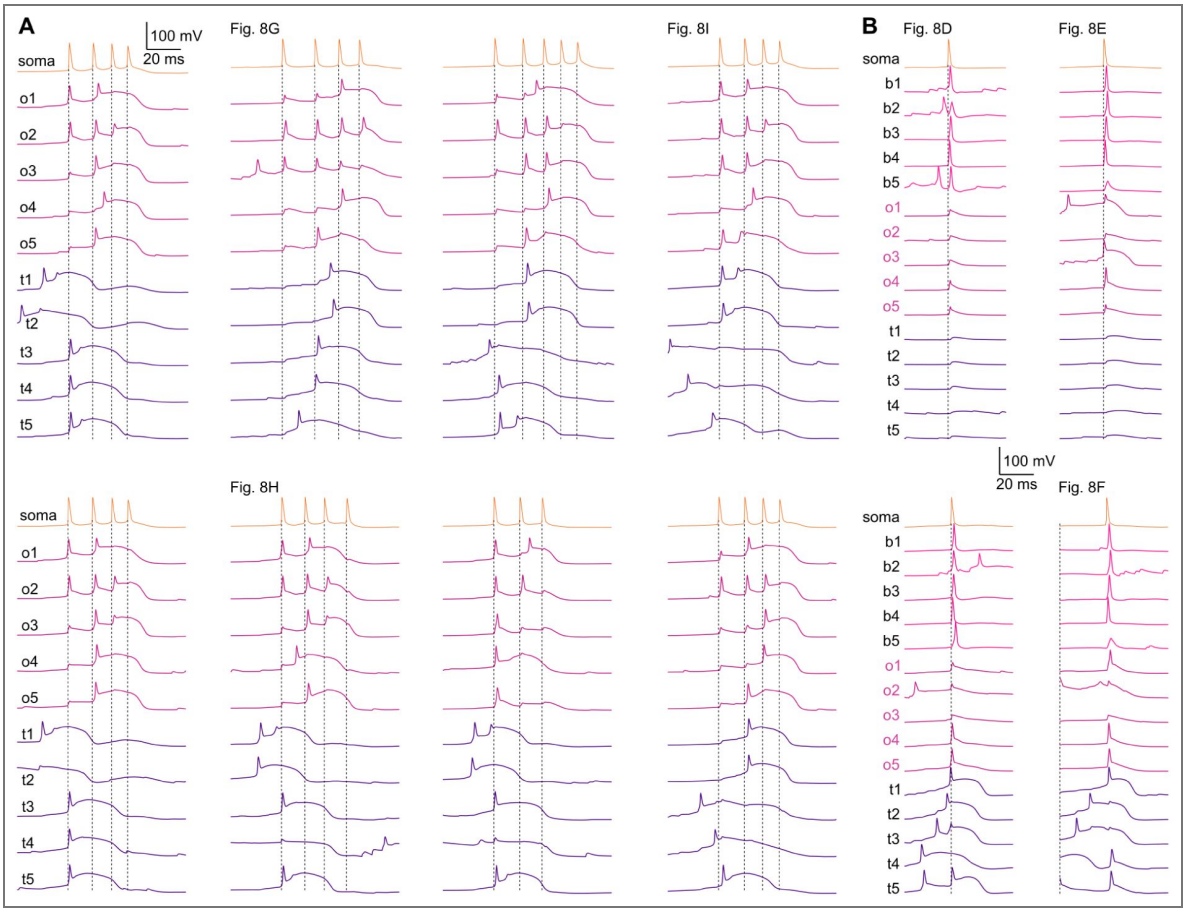

Fig. S3. Further examples of somatic and dendritic Vm dynamics during CSBs and iAPs.

A) Vm response of 5 oblique and 5 tuft branches during 8 different CSB events. The recording locations are the same as in Fig. 4F. The events shown in Fig. 8G-H are indicated above the traces. The timing of the somatic action potentials are marked by dotted vertical lines. **B**) Vm response of 5 oblique and 5 tuft and 5 basal branches during 4 different iAP events. The events shown in Fig. 8D-E are indicated above the traces. Related to Fig. 4.

Fig. S4. Examples of iAPs and CSBs partitioned by current types.

A-C) Somatic (top), distal trunk (middle) and tuft (bottom) currents during iAPs partitioned by current type. The same events are shown as in Fig. 8D-F. **D-F**) Somatic (top), distal trunk (middle) and tuft (bottom) currents during CSBs partitioned by current type. The same events are shown as in Fig. 8G-I.

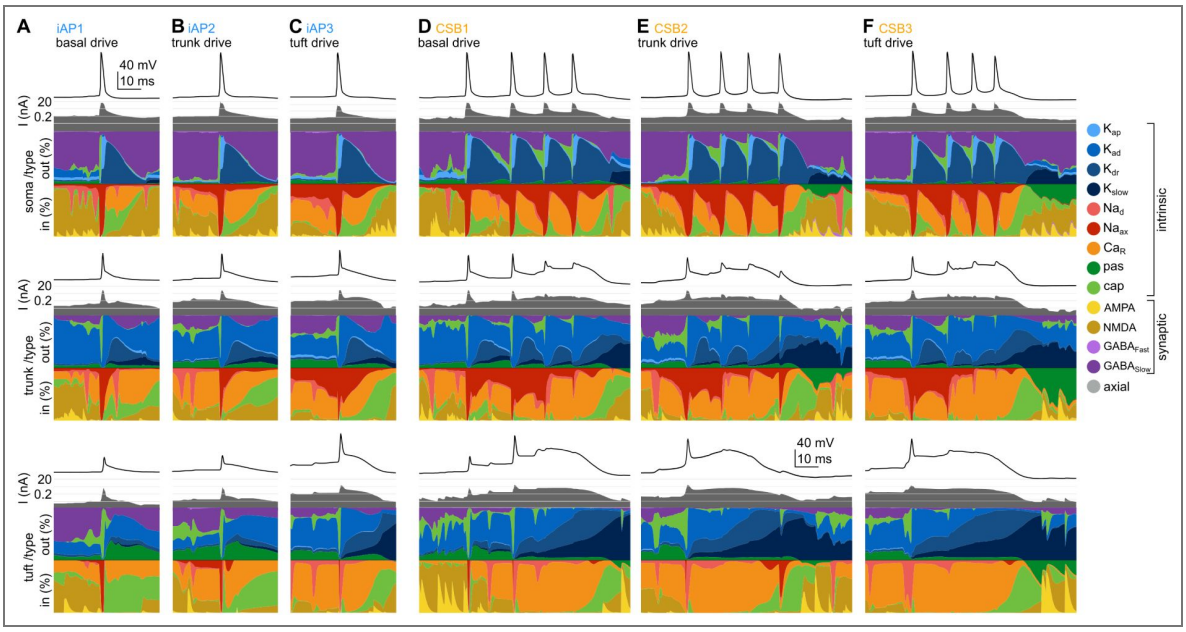

Fig. S5. Simulating optogenetic inhibition of inputs targeting different dendritic domains.

A) The 75% of the input spikes were removed for $N \approx 300$ randomly selected presynaptic inputs targeting the basal (of the $N_{total} \approx 900$ inputs), oblique ($N_{total} \approx 700$) or tuft ($N_{total} \approx 400$) dendrites. In the *basal clustered* case, the number of synapses in the basal input clusters affected by the inhibition were matched to the number of synapses in tuft input clusters. These manipulations significantly reduced both the average number of output spikes and the complex spike bursts (CSBs) per lap (Wilcoxon signed-rank test compared to control, $p < 0.01$ in all cases), with the tuft inhibition having the strongest effect on both spikes and CSBs. Moreover, inhibiting the tuft was more specific than that of the oblique of basal domains as it reduced the number of CSBs to a greater extent than the number of spikes. **B**) The number of CSB events per spikes is most strongly reduced by tuft inhibition. **C**) Simulated optogenetic inhibition also reduced the number of spikes outside of CSBs. This effect was strongest for basal dendrites. Symbols show mean across 16 laps, error bars indicate SE.

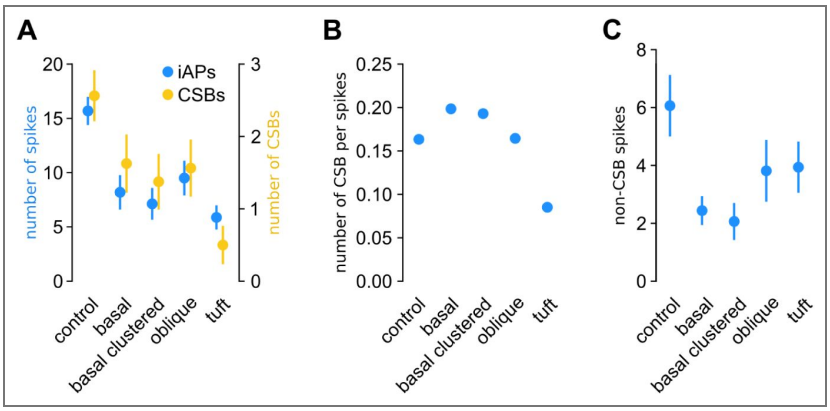

Fig. S6.

Steady-state activation (solid red line) and inactivation (solid blue line) curves of the voltage-gated ion channels expressed in the detailed model (left axis). Dashed lines indicate the time constants of the channels (right axis).

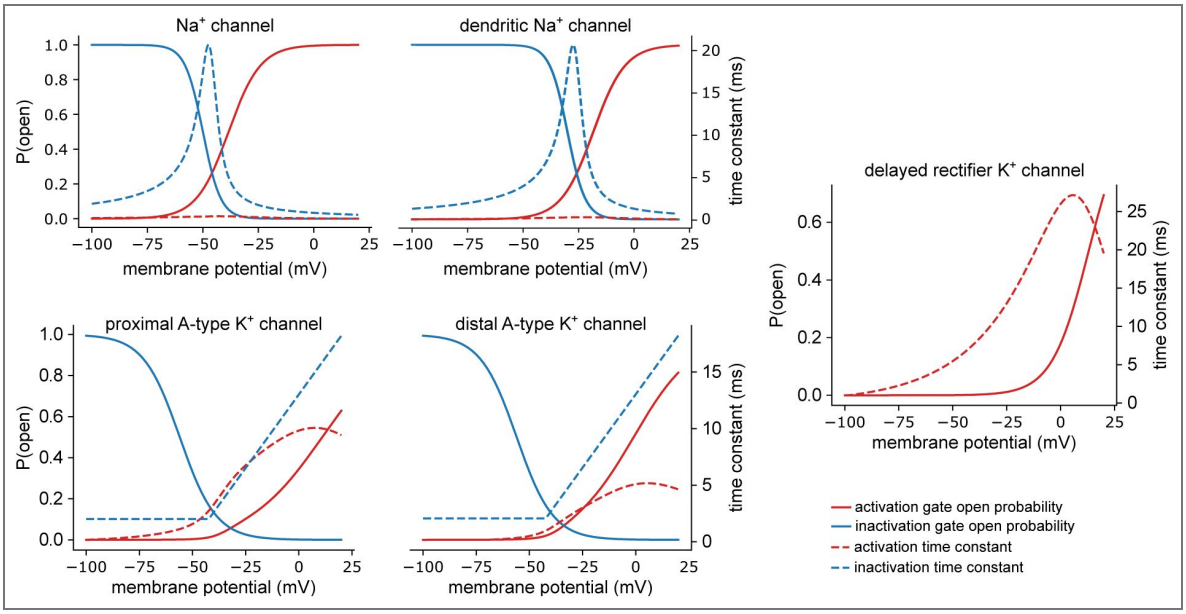

Fig. S7. Summary of synaptic channel kinetics.

A: Time course of excitatory (red) and inhibitory (blue) postsynaptic potentials. We used double exponential kinetics with rise time (τ_1) and decay time (τ_2) constants presented in milliseconds. The reversal potential of the synaptic currents was $E_{\mathrm{AMPA}} = 0\,\mathrm{mV}, E_{\mathrm{NMDA}} = 0\,\mathrm{mV}, E_{\mathrm{GABA_{fast}}} = -65\,\mathrm{mV}\ E_{\mathrm{GABA_{slow}}} = -80\,\mathrm{mV}$ .B : Steady-state activation curve of the NMDA channel.

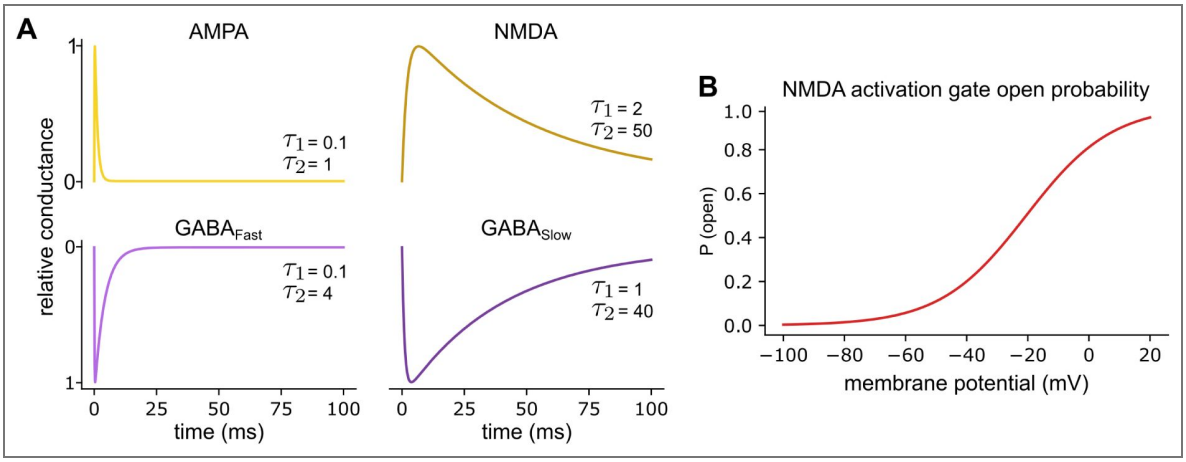

Data availability

The current manuscript is a computational study, so no data have been generated for this manuscript. Modelling code is are available at Github.

Acknowledgements

We thank Judit K Makara, Szabolcs Káli and János Brunner and all members of the Neuronal Signalling and the Biological Computation Research Groups for discussions and for their comments on the manuscript. B.B.U. was supported by the National Research, Development and Innovation Office of Hungary (FK-125324) and by the Hungarian Research Network.

Additional information

Funding

Funder	Grant reference number	Author
National Research, Development and Innovation Office of Hungary	FK-125324	Balazs B Ujfalussy

Author ORCID iDs

Bence Fogel: https://orcid.org/0009-0003-4423-8117
Balázs B Ujfalussy: https://orcid.org/0000-0002-2295-3828

References

Abdelfattah A. S., Zheng J., Singh A., Huang Y.-C., Reep D., Tsegaye G., Tsang A., Arthur B. J., Rehorova M., Olson C. V. L., *et al.* (2023) Sensitivity optimization of a rhodopsin-based fluorescent voltage indicator. *Neuron* **111**:1547-1563. https://doi.org/10.1016/j.neuron.2023.03.009 | PubMed

Adoff M. D., Climer J. R., Davoudi H., Marvin J. S., Looger L. L., Dombeck D. A (2021) The functional organization of excitatory synaptic input to place cells. *Nat Commun* **12**:3558 https://doi.org/10.1038/s41467-021-23829-y | PubMed

Alonso L. M., Marder E (2019) Visualization of currents in neural models with similar behavior and different conductance densities. *eLife* **8**:e42722 https://doi.org/10.7554/eLife.42722 | PubMed

Ariav G., Polsky A., Schiller J (2003) Submillisecond precision of the input-output transformation function mediated by fast sodium dendritic spikes in basal dendrites of CA1 pyramidal neurons. *J Neurosci* **23**:7750-8 https://doi.org/10.1523/jneurosci.23-21-07750.2003 | PubMed

Behabadi B. F., Polsky A., Jadi M., Schiller J., Mel B. W (2012) Location-dependent excita-tory synaptic interactions in pyramidal neuron dendrites. *PLoS computational biology* **8**:e1002599 PubMed | https://doi.org/10.1371/journal.pcbi.1002599

Bicknell B. A., Häusser M (2021) A synaptic learning rule for exploiting nonlinear dendritic computation. *Neuron* **109**:4001-4017. https://doi.org/10.1016/j.neuron.2021.09.044 | PubMed

Bittner K. C., Andrasfalvy B. K., Magee J. C (2012) Ion channel gradients in the apical tuft region of ca1 pyramidal neurons. *PLoS One* **7**:e46652 https://doi.org/10.1371/journal.pone.0046652 | PubMed

Bittner K. C., Grienberger C., Vaidya S. P., Milstein A. D., Macklin J. J., Suh J., Tonegawa S., Magee J. C (2015) Conjunctive input processing drives feature selectivity in hippocampal CA1 neurons. *Nat Neurosci* https://doi.org/10.1038/nn.4062 | PubMed

Bittner K. C., Milstein A. D., Grienberger C., Romani S., Magee J. C (2017) Behavioral time scale synaptic plasticity underlies CA1 place fields. *Science* **357**:1033-1036 https://doi.org/10.1126/science.aan3846 | PubMed

Branco T., Häusser M (2010) The single dendritic branch as a fundamental functional unit in the nervous system. *Current opinion in neurobiology* **20**:494-502 PubMed | https://doi.org/10.1016/j.conb.2010.07.009

Brooks P. F., Davis H. C., Wong-Campos J. D., Cohen A. E (2024) Optical constraints on two-photon voltage imaging. *Neurophotonics* **11**:035007 https://doi.org/10.1117/1.nph.11.3.035007 | PubMed

Cai X., Liang C. W., Muralidharan S., Kao J. P., Tang C. M., Thompson S. M (2004) Unique roles of SK and Kv4.2 potassium channels in dendritic integration. *Neuron* **44**:351-64 https://doi.org/10.1016/j.neuron.2004.09.026 | PubMed

Cohen J. D., Bolstad M., Lee A. K (2017) Experience-dependent shaping of hippocampal CA1 intracellular activity in novel and familiar environments. *eLife* **6** https://doi.org/10.7554/elife.23040 | PubMed

Csicsvári J., Hirase H., Czurkó A., Mamiya A., Buzsáki G (1999) Oscillatory coupling of hippocampal pyramidal cells and interneurons in the behaving rat. *J Neurosci* **19**:274-87 https://doi.org/10.1523/jneurosci.19-01-00274.1999 | PubMed

Destexhe A., Rudolph M., Paré D (2003) The high-conductance state of neocortical neurons in vivo. *Nat Rev Neurosci* **4**:739-51 https://doi.org/10.1038/nrn1198 | PubMed

Dupret D., O'Neill J., Csicsvari J (2013) Dynamic reconfiguration of hippocampal interneuron circuits during spatial learning. *Neuron* **78**:166-80 https://doi.org/10.1016/j.neuron.2013.01.033 | PubMed

Ego-Stengel V., Wilson M. A (2007) Spatial selectivity and theta phase precession in CA1 interneurons. *Hippocampus* **17**:161-74 https://doi.org/10.1002/hipo.20253 | PubMed

Epsztein J., Brecht M., Lee A. K (2011) Intracellular determinants of hippocampal CA1 place and silent cell activity in a novel environment. *Neuron* **70**:109-20 https://doi.org/10.1016/j.neuron.2011.03.006 | PubMed

Fan L. Z., Kim D. K., Jennings J. H., Tian H., Wang P. Y., Ramakrishnan C., Randles S., Sun Y., Thadhani E., Kim Y. S., *et al.* (2023) All-optical physiology resolves a synaptic basis for behavioral timescale plasticity. *Cell* **186**:543-559. https://doi.org/10.1016/j.cell.2022.12.035 | PubMed

Gasparini S., Migliore M., Magee J. C (2004) On the initiation and propagation of dendritic spikes in CA1 pyramidal neurons. *J Neurosci* **24**:11046-56 https://doi.org/10.1523/jneurosci.2520-04.2004 | PubMed

Geiller T., Sadeh S., Rolotti S. V., Blockus H., Vancura B., Negrean A., Murray A. J., Rózsa B., Polleux F., Clopath C., *et al.* (2022) Local circuit amplification of spatial selectivity in the hippocampus. *Nature* **601**:105-109 https://doi.org/10.1038/s41586-021-04169-9 | PubMed

Geiller T., Vancura B., Terada S., Troullinou E., Chavlis S., Tsagkatakis G., Tsakalides P., Ócsai K., Poirazi P., Rózsa B. J., *et al.* (2020) Large-scale 3D two-photon imaging of molecularly identified CA1 interneuron dynamics in behaving mice. *Neuron* **108**:968-983. https://doi.org/10.1016/j.neuron.2020.09.013 | PubMed

Gidon A., Segev I (2012) Principles governing the operation of synaptic inhibition in dendrites. *Neuron* **75**:330-41 https://doi.org/10.1016/j.neuron.2012.05.015 | PubMed

Goetz L., Roth A., Häusser M (2021) Active dendrites enable strong but sparse inputs to determine orientation selectivity. *PNAS* **118**:e2017339118 https://doi.org/10.1073/pnas.2017339118 | PubMed

Golding N. L., Jung H. Y., Mickus T., Spruston N (1999) Dendritic calcium spike initiation and repolarization are controlled by distinct potassium channel subtypes in CA1 pyramidal neurons. *J Neurosci* **19**:8789-98 https://doi.org/10.1523/jneurosci.19-20-08789.1999 | PubMed

González Gómez, Mel J. F., and Poirazi B. W. (2011) Distinguishing linear vs. non-linear integration in CA1 radial oblique dendrites: It's about time. *Front Comput Neurosci* **5**:44 https://doi.org/10.3389/fncom.2011.00044 | PubMed

Grienberger C., Chen X., Konnerth A (2014) NMDA receptor-dependent multidendrite Ca2+ spikes required for hippocampal burst firing in vivo. *Neuron* **81**:1274-81 https://doi.org/10.1016/j.neuron.2014.01.014 | PubMed

Grienberger C., Magee J. C (2022) Entorhinal cortex directs learning-related changes in CA1 representations. *Nature* **611**:554-562 https://doi.org/10.1038/s41586-022-05378-6 | PubMed

Grienberger C., Milstein A. D., Bittner K. C., Romani S., Magee J. C (2017) Inhibitory sup-pression of heterogeneously tuned excitation enhances spatial coding in ca1 place cells. *Nat Neurosci* **20**:417-426 https://doi.org/10.1038/nn.4486 | PubMed

Guet-McCreight A., Skinner F. K (2020) Computationally going where experiments cannot: a dynamical assessment of dendritic ion channel currents during in vivo-like states. *F1000Res* **9**:180 https://doi.org/10.12688/f1000research.22584.2 | PubMed

Häusser M., Mel B (2003) Dendrites: bug or feature?. *Curr Opin Neurobiol* **13**:372-83 https://doi.org/10.1016/s0959-4388(03)00075-8 | PubMed

Hay E., Hill S., Schurmann F., Markram H., Segev I (2011) Models of neocortical layer 5b pyramidal cells capturing a wide range of dendritic and perisomatic active properties. *PLoS Comp Biol* **7**:e1002107 https://doi.org/10.1371/journal.pcbi.1002107 | PubMed

Heredi J., Olah G., Sumegi M., Paul Lukacs I., Aldahabi M., Újfalussy B. B., Makara J. K., Nusser Z (2025) Increased excitatory synapse size in hippocampal place cells compared to silent cells. *PNAS* **122**:e2505322122 https://doi.org/10.1073/pnas.2505322122 | PubMed

Herz A. V., Gollisch T., Machens C. K., Jaeger D (2006) Modeling single-neuron dynamics and computations: a balance of detail and abstraction. *Science* **314**:80-5 https://doi.org/10.1126/science.1127240 | PubMed

Hille B (2001) *Ion Channels of Excitable Membranes* Oxford University Press.

Hines M. L., Carnevale N. T (1997) The neuron simulation environment. *Neural Comput* **9**:1179-209 https://doi.org/10.1162/neco.1997.9.6.1179 | PubMed

Hodgkin A. L., Huxley A. F (1952) A quantitative description of membrane current and its application to conduction and excitation in nerve. *J Physiol* **117**:500-544 https://doi.org/10.1113/jphysiol.1952.sp004764 | PubMed

Hoffman D. A., Magee J. C., Colbert C. M., Johnston D (1997) K+ channel regulation of signal propagation in dendrites of hippocampal pyramidal neurons. *Nature* **387**:869-75 https://doi.org/10.1038/43119 | PubMed

Isomura Y., Sirota A., Ozen S., Montgomery S., Mizuseki K., Henze D. A., Buzsáki G (2006) Integration and segregation of activity in entorhinal-hippocampal subregions by neocortical slow os-cillations. *Neuron* **52**:871-82 https://doi.org/10.1016/j.neuron.2006.10.023 | PubMed

Izhikevich E (2007) *Dynamical Systems in Neuroscience: The Geometry of Excitability and Bursting* The MIT press.

Jarsky T., Roxin A., Kath W. L., Spruston N (2005) Conditional dendritic spike propagation following distal synaptic activation of hippocampal CA1 pyramidal neurons. *Nat Neurosci* **8**:1667-76 https://doi.org/10.1038/nn1599 | PubMed

Kim Y. J., Ujfalussy B. B., Lengyel M (2023) Parallel functional architectures within a single dendritic tree. *Cell Rep* **42**:112386 https://doi.org/10.1016/j.celrep.2023.112386 | PubMed

King B., Rizwan A. P., Asmara H., Heath N. C., Engbers J. D. T., Dykstra S., Bartoletti T. M., Hameed S., Zamponi G. W., Turner R. W (2015) IKCa channels are a critical determinant of the slow AHP in CA1 pyramidal neurons. *Cell Rep* **11**:175-82 https://doi.org/10.1016/j.celrep.2015.03.026 | PubMed

Koch C (1999) *Biophysics of computation* Oxford University Press.

Koch C., Segev I (2000) The role of single neurons in information processing. *Nat Neurosci* **3**:1171-1177 https://doi.org/10.1038/81444 | PubMed

Landau A. T., Park P., Wong-Campos J. D., Tian H., Cohen A. E., Sabatini B. L (2022) Dendritic branch structure compartmentalizes voltage-dependent calcium influx in cortical layer 2/3 pyramidal cells. *eLife* **11**:e76993 https://doi.org/10.7554/eLife.76993 | PubMed

Larkum M. E., Zhu J. J., Sakmann B (1999) A new cellular mechanism for coupling inputs arriving at different cortical layers. *Nature* **398**:338-41 https://doi.org/10.1038/18686 | PubMed

Lee B. H., Park P., Wu X., Wong-Campos J. D., Xu J., Xiong M., Qi Y., Huang Y.-C., Itkis D. G., Plutkis S. E., *et al.* (2026) Fast dendritic excitations primarily mediate back-propagation in ca1 pyramidal neurons during behavior. *bioRxiv* https://doi.org/10.64898/2026.01.03.696606 | PubMed

Li B., Routh B. N., Johnston D., Seidemann E., Priebe N. J (2020) Voltage-gated intrinsic conductances shape the input-output relationship of cortical neurons in behaving primate V1. *Neuron* **107**:185-196. https://doi.org/10.1016/j.neuron.2020.04.001 | PubMed

Liao Z., Gonzalez K. C., Li D. M., Yang C. M., Holder D., McClain N. E., Zhang G., Evans S. W., Chavarha M., Simko J., *et al.* (2024) Func-tional architecture of intracellular oscillations in hippocampal dendrites. *Nat Commun* **15**:6295 https://doi.org/10.1038/s41467-024-50546-z | PubMed

Linaro D., Levy M. J., Hunt D. L (2022) Cell type-specific mechanisms of information trans-fer in data-driven biophysical models of hippocampal CA3 principal neurons. *PLoS Comput Biol* **18**:e1010071 https://doi.org/10.1371/journal.pcbi.1010071 | PubMed

London M., Häusser M (2005) Dendritic computation. *Annu Rev Neurosci* **28**:503-32 https://doi.org/10.1146/annurev.neuro.28.061604.135703 | PubMed

Losonczy A., Magee J. C (2006) Integrative properties of radial oblique dendrites in hippocampal CA1 pyramidal neurons. *Neuron* **50**:291-307 https://doi.org/10.1016/j.neuron.2006.03.016 | PubMed

Magee J. C., Carruth M (1999) Dendritic voltage-gated ion channels regulate the action potential firing mode of hippocampal ca1 pyramidal neurons. *J Neurophysiol* **82**:1895-901 https://doi.org/10.1152/jn.1999.82.4.1895 | PubMed

Magee J. C., Johnston D (1995) Characterization of single voltage-gated Na+ and Ca2+ channels in apical dendrites of rat CA1 pyramidal neurons. *J Physiol* **487**:67-90 https://doi.org/10.1113/jphysiol.1995.sp020862 | PubMed

Magó Á., Kis N., Lükő B., Makara J. K (2021) Distinct dendritic Ca2+ spike forms produce opposing input-output transformations in rat ca3 pyramidal cells. *eLife* **10** https://doi.org/10.7554/elife.74493 | PubMed

Megias M., Emri Z., Freund T. F., Gulyas A. I (2001) Total number and distribution of inhibitory and excitatory synapses on hippocampal CA1 pyramidal cells. *Neuroscience* **102**:527-40 https://doi.org/10.1016/s0306-4522(00)00496-6 | PubMed

Meszéna D., Barlay A., Boldog P., Furuglyás K., Cserpán D., Wittner L., Ulbert I., Somogyvári Z (2023) Seeing beyond the spikes: reconstructing the complete spatiotemporal membrane potential distribution from paired intra- and extracellular recordings. *J Physiol* **601**:3351-3376 https://doi.org/10.1113/jp283550 | PubMed

Metz A. E., Jarsky T., Martina M., Spruston N (2005) R-type calcium channels contribute to afterdepolarization and bursting in hippocampal CA1 pyramidal neurons. *J Neurosci* **25**:5763-73 https://doi.org/10.1523/jneurosci.0624-05.2005 | PubMed

Milstein A. D., Bloss E. B., Apostolides P. F., Vaidya S. P., Dilly G. A., Zemelman B. V., Magee J. C (2015) Inhibitory gating of input comparison in the ca1 microcircuit. *Neuron* **87**:1274-89 https://doi.org/10.1016/j.neuron.2015.08.025 | PubMed

Naud R., Sprekeler H (2018) Sparse bursts optimize information transmission in a multiplexed neural code. *PNAS* **115**:E6329-E6338 https://doi.org/10.1073/pnas.1720995115 | PubMed

Nicholson D. A., Trana R., Katz Y., Kath W. L., Spruston N., Geinisman Y (2006) Distance-dependent differences in synapse number and ampa receptor expression in hippocampal ca1 pyramidal neurons. *Neuron* **50**:431-42 https://doi.org/10.1016/j.neuron.2006.03.022 | PubMed

O'Hare J. K., Wang J., Shala M. D., Polleux F., Losonczy A (2025) Distal tuft dendrites predict properties of new hippocampal place fields. *Neuron* **113**:1969-1982. https://doi.org/10.1016/j.neuron.2025.03.029 | PubMed

Palmer L. M., Shai A. S., Reeve J. E., Anderson H. L., Paulsen O., Larkum M. E (2014) NMDA spikes enhance action potential generation during sensory input. *Nature Neuroscience* **17**:383-390 https://doi.org/10.1038/nn.3646 | PubMed

Park P., Wong-Campos J. D., Itkis D. G., Lee B. H., Qi Y., Davis H. C., Antin B., Pasarkar A., Grimm J. B., Plutkis S. E., *et al.* (2025) Den-dritic excitations govern back-propagation via a spike-rate accelerometer. *Nat Commun* **16**:1333 https://doi.org/10.1038/s41467-025-55819-9 | PubMed

Payeur A., Béïque J.-C., Naud R (2019) Classes of dendritic information processing. *Curr Opin Neurobiol* **58**:78-85 https://doi.org/10.1016/j.conb.2019.07.006 | PubMed

Pearl J (2009) *CAUSALITY Models, Reasoning, and Inference* Cambridge University Press.

Poirazi P., Brannon T., Mel B. W (2003) Arithmetic of subthreshold synaptic summation in a model CA1 pyramidal cell. *Neuron* **37**:977-87 https://doi.org/10.1016/s0896-6273(03)00148-x | PubMed

Qian F. K., Li G., Lipshutz D., Romani S., Magee J. C (2025) Memory traces bias new learning for hippocampal generalization. *bioRxiv* https://doi.org/10.1101/2025.11.24.690297

Rolotti S. V., Blockus H., Sparks F. T., Priestley J. B., Losonczy A (2022) Reorganization of ca1 dendritic dynamics by hippocampal sharp-wave ripples during learning. *Neuron* **110**:977-991. https://doi.org/10.1016/j.neuron.2021.12.017 | PubMed

Sáray S., Rössert C. A., Appukuttan S., Migliore R., Vitale P., Lupascu C. A., Bologna L. L., Van Geit W., Romani A., Davison A. P., *et al.* (2021) Hippounit: A software tool for the automated testing and systematic comparison of detailed models of hippocampal neurons based on electrophysiological data. *PLoS Comput Biol* **17**:e1008114 https://doi.org/10.1371/journal.pcbi.1008114 | PubMed

Sheffield M. E. J., Adoff M. D., Dombeck D. A (2017) Increased prevalence of calcium transients across the dendritic arbor during place field formation. *Neuron* **96**:490-504. https://doi.org/10.1016/j.neuron.2017.09.029 | PubMed

Sheffield M. E. J., Dombeck D. A (2015) Calcium transient prevalence across the dendritic arbour predicts place field properties. *Nature* **517**:200-4 https://doi.org/10.1038/nature13871 | PubMed

Skaggs W. E., McNaughton B. L., Wilson M. A., Barnes C. A (1996) Theta phase precession in hippocampal neuronal populations and the compression of temporal sequences. *Hippocampus* **6**:149-72 https://doi.org/10.1002/(sici)1098-1063(1996)6:2<149::aid-hipo6>3.0.co;2-k | PubMed

Smith S. L., Smith I. T., Branco T., Häusser M (2013) Dendritic spikes enhance stimulus selectivity in cortical neurons in vivo. *Nature* **503**:115-20 https://doi.org/10.1038/nature12600 | PubMed

Spruston N., Schiller Y., Stuart G., Sakmann B (1995) Activity-dependent action potential invasion and calcium influx into hippocampal CA1 dendrites. *Science* **268**:297-300 https://doi.org/10.1126/science.7716524 | PubMed

Stuart G. J., Häusser M (2001) Dendritic coincidence detection of EPSPs and action potentials. *Nat Neurosci* **4**:63-71 https://doi.org/10.1038/82910 | PubMed

Takahashi H., Magee J. C (2009) Pathway interactions and synaptic plasticity in the dendritic tuft regions of CA1 pyramidal neurons. *Neuron* **62**:102-11 https://doi.org/10.1016/j.neuron.2009.03.007 | PubMed

Tasciotti S., Iascone D. M., Chavlis S., Hammond L., Katz Y., Losonczy A., Polleux F., Poirazi P (2025) From morphology to computation: How synaptic organization shapes place fields in ca1 pyramidal neurons. *bioRxiv* https://doi.org/10.1101/2025.05.30.657022 | PubMed

Tran-Van-Minh A., Abrahamsson T., Cathala L., DiGregorio D. A (2016) Differential dendritic integration of synaptic potentials and calcium in cerebellar interneurons. *Neuron* **91**:837-850 https://doi.org/10.1016/j.neuron.2016.07.029 | PubMed

Ujfalussy B. B., Makara J. K (2020) Impact of functional synapse clusters on neuronal response selectivity. *Nat Commun* **11**:1413 https://doi.org/10.1038/s41467-020-15147-6 | PubMed

Ujfalussy B. B., Makara J. K., Lengyel M., Branco T (2018) Global and multiplexed dendritic computations under in vivo-like conditions. *Neuron* **100**:579-592 https://doi.org/10.1016/j.neuron.2018.08.032 | PubMed

Vaidya S. P., Li G., Chitwood R. A., Li Y., Magee J. C (2025) Formation of an expanding memory representation in the hippocampus. *Nat Neurosci* **28**:1510-1518 https://doi.org/10.1038/s41593-025-01986-3 | PubMed

Valero M., Zutshi I., Yoon E., Buzsáki G (2022) Probing subthreshold dynamics of hippocampal neurons by pulsed optogenetics. *Science* **375**:570-574 https://doi.org/10.1126/science.abm1891 | PubMed

Weber J. P., Andrásfalvy B. K., Polito M., Magó Á., Ujfalussy B. B., Makara J. K (2016) Location-dependent synaptic plasticity rules by dendritic spine cooperativity. *Nat Commun* **7**:11380 https://doi.org/10.1038/ncomms11380 | PubMed

Wei D. S., Mei Y. A., Bagal A., Kao J. P., Thompson S. M., Tang C. M (2001) Compart-mentalized and binary behavior of terminal dendrites in hippocampal pyramidal neurons. *Science* **293**:2272-5 https://doi.org/10.1126/science.1061198 | PubMed

Wen J. H., Sorscher B., Aery Jones E. A., Ganguli S., Giocomo L. M (2024) One-shot entorhinal maps enable flexible navigation in novel environments. *Nature* **635**:943-950 https://doi.org/10.1038/s41586-024-08034-3 | PubMed

Wilson M. A., McNaughton B. L (1993) Dynamics of the hippocampal ensemble code for space. *Science* **261**:1055-1058 https://doi.org/10.1126/science.8351520 | PubMed

Wilson M. A., McNaughton B. L (1994) Reactivation of hippocampal ensemble memories during sleep. *Science* **265**:676-679 PubMed | https://doi.org/10.1126/science.8036517

Witter M. P., Groenewegen H. J., Lopes da Silva F. H., Lohman A. H. (1989) Functional organization of the extrinsic and intrinsic circuitry of the parahippocampal region. *Prog Neurobiol* **33**:161-253 https://doi.org/10.1016/0301-0082(89)90009-9 | PubMed

Peer reviews

Reviewer #1 (Public review):

Summary

Fogel & Ujfalussy report an extension of a visualization tool that was originally designed to enable an understanding of detailed biophysical neuron models. Named "extended currentscape", this new iteration enables visual assessment of individual currents across a neuron's spatially extended dendritic arbor with simultaneous readout of somatic currents and voltage. The overall aim was to permit a visually intuitive understanding for how a model neuron's inputs determine its output. This goal was worthwhile and the authors achieved it. Demonstrating the utility of extended currentscape, the authors leverage their models to generate interesting and detailed biophysical insights into widely studied neurophysiological phenomena with clear behavioral relevance. Overall, this study provides a valuable and well-characterized biophysical modeling resource to the neuroscience community.

Strengths

The authors significantly extended a previously published open-source biophysical modeling tool. Beyond providing important new capabilities, the potential impact of extended currentscape is boosted by its integration with preexisting resources in the field.

In keeping with the authors' goal to provide an approachable platform with intuitive visualizations of how current flows through neurons, the manuscript is approachable to non-computationalists. In particular, a dedicated glossary and elegant illustrations in Figure 2 boost accessibility for biologists.

Extended currentscape produces intriguing and detailed predictions spanning neurophysiological phenomena such as local dendritic spikes, complex spike generation, and feature selectivity (hippocampal place fields). By triggering analysis of modeled synaptic inputs on these events, the authors trace their origins from dendritic integration to synaptic input patterns.

The authors cleverly apply a graph theoretical approach to efficiently model bidirectional current flow throughout a neuron's dendritic arbor. As a result, extended currentscape can run on a standard personal computer.

The code is well-documented and freely available via GitHub.

Weaknesses

While extended currentscape meets its objective of modeling and illustrating the propagation of axial currents throughout a model neuron in great detail, it requires simulation and measurement of synaptic input currents. For this reason, there currently exists a very high technical barrier to conclusively test its intriguing predictions: simultaneous readout of synaptic inputs throughout a neuron's dendritic arbor. Mitigating this weakness, the authors propose a relatively more feasible alternative approach in Discussion: simultaneous voltage imaging of dendrites and their soma while estimating synaptic inputs from the distributions of voltage dynamics along individual dendritic branches.

https://doi.org/10.7554/eLife.108352.2.sa2

Reviewer #2 (Public review):

The electrical activity of neurons and neuronal circuits is dictated by the concerted activity of multiple ionic currents. Because directly investigating these currents experimentally is not possible with current methods, researchers rely on biophysical models to develop hypotheses and intuitions about their dynamics. Models of neural activity produce large amounts of data that are hard to visualize and interpret. The currentscape technique helps visualize the contributions of currents to membrane potential activity, but it is limited to model neurons without spatial properties. The extended currentscape technique overcomes this limitation by tracking the contributions of the different currents from distant locations. This extension allows tracking not only the types of currents that contribute to the activity in a given location, but also visualizing the spatial region where the currents originate. The procedure is first illustrated in a simple setting that allows testing its validity in an intuitive situation where a cell with an apical trunk and two dendritic branches responds to synaptic inputs. The procedure is then applied to study the initiation of complex spike bursts in a model hippocampal place cell.

The extended currentscape method represents a significant improvement over the original technique, which is already utilized by several research groups. By enabling the analysis of current contributions in spatially extended models, this technique provides a new lens for investigating neuronal and circuit dynamics and will be of use to the modeling community.

Comments on revisions:

The changes in Figure 2 greatly improved the manuscript.

https://doi.org/10.7554/eLife.108352.2.sa1

Author response:

The following is the authors' response to the original reviews.

Public Reviews:

Reviewer #1 (Public review):

Summary:

Fogel & Ujfalussy report an extension of a visualization tool that was originally designed to enable an understanding of detailed biophysical neuron models. Named "extended currentscape", this new iteration enables visual assessment of individual currents across a neuron's spatially extended dendritic arbor with simultaneous readout of somatic currents and voltage. The overall aim was to permit a visually intuitive understanding for how a model neuron's inputs determine its output. This goal was worthwhile and the authors achieved it. Their manuscript makes two additional contributions of note: (1) a clever algorithmic approach to model the axial propagation of ionic currents (recursively traversing acyclic graph subsections) and (2) interesting, albeit not easily testable, insights into important neurophysiological phenomena such as complex spike generation and place field dynamics. Overall, this study provides a valuable and well-characterized biophysical modeling resource to the neuroscience community.

Strengths:

The authors significantly extended a previously published open-source biophysical modeling tool. Beyond providing important new capabilities, the potential impact of "extended currentscape" is boosted by its integration with preexisting resources in the field.

The code is well-documented and freely available via GitHub.

The author's clever portioning algorithm to relate dendritic/synaptic currents to somatic yielded multiple intriguing observations regarding when and why CA1 pyramidal neurons fire complex spikes versus single action potentials. This topic carries major implications for how the hippocampus represents and stores information about an animal's environment.

Weaknesses:

While extended currentscape is clearly a valuable contribution to the neuroscience community, this reviewer would argue that it is framed in a way that oversells its capabilities. The Abstract, Introduction, Results, and Methods all contain phrases implying that extended currentscape infers dendritic/synaptic currents contributing to somatic output., i.e. backwards inference of unknown inputs from a known output. This is not the case; inputs are simulated and then propagated through the model neuron using a clever partitioning algorithm that essentially traverses a biologically undirected graph structure by treating it like a time series of tiny directed graphs. This is an impressive solution, but it does not infer a neuron's input structure.

We are sorry if our text could be interpreted as if we were inferring unobserved inputs from the known outputs. This was not intentional and we were unaware of the possibility of such interpretation.

In fact, at the beginning of the Results, we started the description of the extended currentscape method by explicitly stating that we need to measure the input currents: “Our method … requires measuring the membrane and axial currents throughout the dendritic tree of a neuron (in every node of the circuit)”.

To further clarify that our method starts with measuring the input currents, we made this information explicit already in the abstract (“Our approach relies on the iterative

decomposition of the axial current flowing between neighbouring compartments in proportion to the underlying membrane currents measured in the model."), and in the Introduction ("Even if the membrane currents are known, studying the impact of particular ion channels on the neuronal response in such a dynamical system under *in vivo* conditions is hindered by two major obstacles"). We also rewrote several parts of the text to remove any phrases that could imply the inference of the inputs (line 568). We believe that after clarifying this at the beginning of the paper, the readers will not misinterpret our descriptions later in the text.

> *Because a directed acyclic graph architecture is shown in Figure 2, it is unintuitive that the authors can infer bidirectional current flow, e.g. Figure 3 showing current flowing from basal dendrites and axon to soma, and further towards the apical dendrites. This is explained in Methods, but difficult to parse from Results amidst lots of rather abstract jargon (target, reference, collision, compartment). Figure 2 would have presented an opportunity to clearly illustrate the author's portioning algorithm by (1) rooting it in the exact morphology of one of their multicompartmental model neurons and (2) illustrating that "target" and "reference" have arbitrary morphological meanings; they describe the direction of current flow which is reevaluated at each time step.*

We thank for this comment. We agree that the concepts introduced here to explain our method are rather abstract and could be difficult to understand. To help the reader we followed the instructions of Reviewer and redesigned Fig. 2 to provide a step by step explanation of the extended currentscape method. In particular,

We used a simpler model where the structure of the graph can be directly related to the morphology of the model.

We show that the target node can connect multiple subtrees with axial currents flowing in different directions. We explain that in this case the inward and the outward subtrees are pruned and partitioned separately.

We provide a glossary in Table 1 to ensure that the readers can follow our description and do not get lost amidst lots of rather abstract jargon.

We also clarified that although the target compartment is chosen arbitrarily by the user, it remains the same for all time points throughout the analysis.

> *Analyses in Figure 7, C and D, are insightfully devised and illuminating. However, they could use some reconciliation with Figure 5 regarding initiation of individual APs versus CSBs within place fields.*

We thank the reviewer for the positive comments and also for pointing out the potential source of misunderstanding. We slightly changed the text at Fig 5 to emphasize that this is a single example trial, and we added the following sentence to the paragraph describing Fig 7CD: "Consequently, the somatic current dynamics before the iAP and the CSB presented in Fig 5Cc-Dd can be regarded as illustrative samples from a broad distribution, but the differences observed between them are not representative.}"

> *The intriguing observations generated by extended currentscape also point to its main weakness, which the authors openly acknowledge: as of now, no experimental methods exist to conclusively tests its predictions.*

We agree with the Reviewer that not being able to apply our extended currentscape method to reveal the current types driving real neurons recorded *in vivo* is currently a weakness of our approach. However, we would like to emphasize that it may be feasible to use it to estimate the spatial distribution of the membrane currents driving the cell based on *in vivo* voltage imaging data, as we briefly outline in the discussion.

> ***Reviewer #2 (Public review):***
>
> *Summary*
>
> *The electrical activity of neurons and neuronal circuits is dictated by the concerted activity of multiple ionic currents. Because directly investigating these currents experimentally isn't possible with current methods, researchers rely on biophysical models to develop hypotheses and intuitions about their dynamics. Models of neural activity produce large amounts of data that is hard to visualize and interpret. The currentscape technique helps visualize the contributions of currents to membrane potential activity, but it's limited to model neurons without spatial properties. The extended currentscape technique overcomes this limitation by tracking the contributions of the different currents from distant locations. This extension allows tracking not only the types of currents that contribute to the activity in a given location, but also visualizing the spatial region where the currents originate. The method is applied to study the initiation of complex spike bursts in a model hippocampal place cell.*
>
> *Strengths. >*
>
> *The visualization method introduced in this work represents a significant improvement over the original currentscape technique. The extended currentscape method enables investigation of the contributions of currents in spatially extended models of neurons and circuits. >*
>
> *Weaknesses.*
>
> *The case study is interesting and highlights the usefulness of the visualization method. A simpler case study may have been sufficient to exemplify the method, while also allowing readers to compare the visualizations against their own intuitions of how currents should flow in a simpler setting. >*

We thank the reviewer for this comment. In fact we had been also considering to include a simpler case study to illustrate the extended currentscape method in the original submission. In accordance with the comments from Reviewer 1, we now use a simple model to introduce the concepts in Figure 2 and provide a few examples where the reader can compare the results with their own intuition in simpler cases.

> ***Recommendations for the authors:***
>
> ***Reviewing Editor Comments:***
>
> *(1) Model complexity vs. intuition/validation. The case study relies on a very complex CA1 model, making it difficult to build intuition about current flow and to validate the visualization. Inclusion of a simpler benchmark (e.g., soma plus a dendrite with two branches, fewer compartments) is recommended to demonstrate how the extended currentscape behaves in a more tractable setting.*

Inspired by the suggestions of the Reviewers, we modified Figure 2 and now first use a simple model with a soma and a dendrite with two branches to introduce the concepts of our analysis. We start with a few examples where the reader can compare the results with their own intuition in simpler cases.

> *(2) Rationale and citations for input structure. The in vivo-like input design (untuned inhibition; 12 co-tuned excitatory clusters with large conductances; the goal of generating place fields) would benefit from a more explicit rationale and substantially more literature support. Alternative plausible scenarios (e.g., distributed co-tuned inputs and homosynaptic plasticity) should be articulated, and choices situated within the*

> *experimental literature on CA1 excitation/inhibition, including tuning and anti-tuning results.*

We extended the paragraph in the Results describing the input structure and added the most important references there. We added further references to the Methods section where we argue that "Reliable place cell tuning can be achieved by functional synaptic clustering without increased excitatory drive in the place field (Ujfalussy and Makara 2020) or via strong excitatory drive without input clustering (Grienberger et al., 2017, Ujfalussy and Makara, 2020). However, experimental data indicates that both of these mechanisms are present and contribute to the activity of place cells (Adoff et al., 2021,Tasciotti et al., 2025)" and "although interneurons can display spatial tuning, they typically have a broad tuning with low selectivity (Ego-Stengel et al., 2007, Dupret et al., 2013, Geiller et al., 2020). A weak disinhibition within the place field can also contribute to the selective firing of place cells (Geiller et al., 2022, Valero et al., 2022), this was not necessary for place cell activity in novel environments (Geiller et al., 2022) and the overall inhibitory input to place cells is largely untuned (Grienberger et al., 2017)."

> *(3) Scope of PCA-based claims. The interpretations derived from the PCA analysis appear broader than warranted, given subcellular heterogeneity and the dominance of somatic action potential variance. These claims should be tempered with more explicit statements about what PCA can and cannot resolve in this context.*

We thank the Reviewer for the opportunity and encouragement to clarify this part of the text. We agree with the Editor and the Reviewers that the results of the PCA analysis can not be used to support claims regarding the presence or the absence of independent dendritic events. In fact, we aimed to use it as an illustration that global activity tends to dominate PCA analysis even when the "neuron is mainly driven by strong, functionally clustered synaptic inputs to a few dendritic branches". We acknowledge that we did not formulate this point clearly in the original submission. Therefore we substantially rewrote this part of the Results and performed additional analysis to clarify that there is a substantial amount of soma-independent dendritic activity in our model that remains invisible for a PCA based analysis.

> ***Reviewer #1 (Recommendations for the authors):***
>
> *Major concerns:*
>
> *(1) Depolarization-inactivated K+ may be an important consideration to model burst-firing.*

Our current model includes 2 kinds of transient K+ channels that show inactivation after depolarization: a proximal and a distal type, as the original model in Jarsky et al., 2005. We now made this explicit in the main text (line 178).

> *(2) Description of the in vivo-like model's excitatory and inhibitory input structure needs many more citations of biological studies to communicate rationale for the author's decisions, e.g. untuned inhibitory neurons, organization of a subset of excitatory inputs into 12 function synaptic clusters with co-tuned presynaptic neurons and outsized synaptic conductances. The goal is clearly to create CA1 pyramidal neurons with place fields, which would be helpful to state upfront. But additionally, (a) place fields could arise from homosynaptic potentiation of distributed co-tuned excitatory inputs (e.g., Bittner, et al. 2017 study describing BTSP made no assumptions) and (b) CA1 inhibitory interneurons can be spatially tuned (Ego-Stengel & Wilson, 2006; Wilent & Nitz, 2007; Geiller, et al. 2020) and even anti-tuned (Geiller, et al. 2021).*

We thank the Reviewer for pointing out the lack of appropriate references in this section. We made the following changes in the manuscript:

(1) Stated explicitly that the goal was to create place cell activity.

(2) Added references to the main text to justify our choices of the inputs (lines 234-241).

(3) We included a longer rationale for the choice of synaptic clusters and the lack of inhibitory (anti-)tuning in the Methods section, describing the neuron model. In brief, Adoff et al., 2021 reported more clustering of excitatory inputs within the place field. In our model, the degree of clustering is somewhat larger than the clusters reported. Although inhibitory neurons can be tuned, their tuning is much weaker than that of place cells and seems to play only a minor role in the generation of place fields (Grienberger et al., 2017). The presence of inhibitory anti-tuning is controversial: although Geiller et al., 2021 reported weak (~10%) anti-tuning, they did not find it in novel environments, indicating that it is not needed for spatially selective activity (lines 628-646).

> *(3) Interpretation of principal component-based analyses shown in Figure 4 could be toned down. As written in section "CSBs in the CA1 pyramidal neuron", it sounds like CA1 pyramidal neuron dendrites display minimal autonomous activity. However, PCA does not seem well-suited to address the heterogeneity of subcellular voltage dynamics over physiologically relevant timescales. Somatic action potentials, and their backpropagation/modulation of dendritic voltage, would of course explain a very large fraction of variance. However, if local dendritic events summate over fine timescales to initiate somatic firing, it is hard to imagine this important nuance being detected. On the other hand, it is hard to imagine single dendritic branches driving robust somatic firing except in the relatively extreme situation in which large numbers of synapses synchronously drive the same branch to initiate a local Ca2+ spike (Figure 3, A-C).*

We agree with the reviewer that PCA can not reveal the potential dendritic origin of somatic APs, and thus is not suitable to assess the role of local dendritic spikes in shaping the output of the cell. We wanted to highlight here that even in cells with excitable dendrites driven by strong, local input clusters, exhibiting frequent local dendritic spikes, the dendritic membrane potential dynamics will be dominated by global fluctuations with surprisingly little sign of local dynamics in the PCA components. As the reviewer also pointed out, this may not be surprising as local events either remain spatially restricted and thus contribute little to the overall variability of the dendritic Vm or they initiate somatic APs and will thus be counted as global events.

To demonstrate the high propensity of local dendritic events, we analysed local Vm peaks in dendritic branches and found that ~7.6% of the peaks were not coupled to somatic APs.

Although this number could seem low, we emphasize that most of the 92.4% of the dendritic peaks coupled to APs potentially reflect the backpropagation of the same somatic events to multiple dendritic sites. To confirm this, we performed an additional analysis measuring the spatial extent (number of branches involved) of the individual dendritic events. We found that 90% of the events remained local, restricted to a few dendritic branches, while 10% of the events were global, associated with BAPs and involving the majority of the dendritic tree. Interestingly, these global events dominate the PCA analysis and are responsible for >90% of the dendritic Vm peaks. These results are included in a new panel in Figure 4H.

We conclude that, “this way, although only 10% of the dendritic Vm events were associated with bAPs, they were ~60-times larger than local events and they dominated the PCA analysis even in the presence of local regenerative dendritic events driven by strong, functionally clustered synaptic inputs.” We believe that this model and analysis could serve as an important benchmark for future experimental studies investigating the structure of membrane potential correlations in *in vivo* voltage imaging data (Lee et al., 2026).

> *(4) One suggestion would be to display more data as shown in Figure 4F, with a longer X axis to clarify the temporal relationship between local dendritic spikes and the first somatic action potential.*

We added a few more examples including the CSBs presented in Fig8G-I as a new supplementary Figure S4. We also slightly extended the x-axis on this supplementary figure as the reviewer requested.

> *If the models indicate that passively filtered EPSPs drive most somatic action potentials, as seems to be the case in Figure 5, then this would also be helpful to show as in Figure 4F.*

In Fig 5 we showed two examples of isolated APs. The first AP was indeed driven by passively filtered EPSPs. The second one was preceded and possibly caused by a dendritic spike, as highlighted by the black arrowhead labelled c in Fig. 5Cc. We further analysed the currents driving iAPs in Fig 7B and C, and found that there is considerable heterogeneity in the magnitude of the dendritic Na currents driving the soma before action potentials. Figure 8 and Figure S3 (now Fig. S5) show further examples for iAPs driven either by passively filtered EPSPs or dendritic spikes. We also included these examples in the new supplementary Figure S4.

> *(5) Another suggestion would be to use one-hot vectors containing onset times of different event types, since this would divorce the amplitude/duration of events from their influence over total variance.*

In this paper our goal was to illustrate the ability of the extended currentscape method to reveal the origin of the axial currents driving neuronal activity. In Fig. 4, our primary intention was to characterize the membrane potential response of the model in a way that is easily comparable with experimental data. To further quantify the frequency of local events, we added a new panel showing the spatial extent of dendritic events (Fig. 4H). To make our model more comparable with recent publications, we also calculated two additional metrics used to evaluate the relationship between somatic and dendritic activity (Fig 4I-J). We hope that these additional analyses help the reader to characterize the prevalence and impact of local dendritic events on somatic activity.

> *(6) From section "Input conditions for complex spike burst generation", paragraph 2: "Note that synapse density, the ion channel mechanisms and the input statistics are identical for tuft and oblique branches,...". The authors should justify this parameterization given the numerous known differences between tuft and oblique branches in both of these regards and acknowledge accompanying interpretational caveats.*

We agree with the reviewer that experimental data demonstrated several significant differences between the tuft and oblique branches regarding both the inputs they receive and the way they process it. However, in the present paper we chose not to include these differences for several reasons:

Here we aimed to focus on the abilities of the dendritic currentscape methods and use CSBs as a case study to illustrate how dendritic currentscape can reveal the membrane currents underlying complex neuronal responses.

Currently there is no CA1PN model that would be able to reproduce all data regarding tuft and oblique integration and would be able to fire calcium spikes. We only wanted to make minimal modifications to the existing CA1PN model to make it capable of generating Ca-spikes and CSBs. We are currently working towards developing and extensively testing a new model, examining the role of these regional differences in CSB generation.

Although there is information regarding input statistics and dendritic physiology in the literature, many of the relevant parameters are underconstrained. We wanted to avoid overfitting by keeping the model simple.

By maintaining identical inputs and ion channel distribution we can distinctly highlight the special role of tuft morphology in CSB generation. Altering the inputs or the ion channel density for the tuft would make the interpretation more ambiguous, and elucidating the specific role of the different factors in CSB generation is the subject of future investigations.

In sum, although we acknowledge that our model does not reflect the full complexity of CA1 PNs and its inputs, we regard this simplicity as a useful feature of the model. We added a section discussing potential future extensions of the model and highlighting interpretational caveats in the discussion (lines 482-490).

> *(7) Given the debate in the field regarding the level of functional autonomy present in dendrites, the authors' finding that dendritic voltage largely tracks that of the soma (though see concern above re: PCA), and their access to specific currents, the authors have an important opportunity investigate the divergence between Ca2+ and voltage sensors as reporters of dendritic activity.*
>
> *For instance, why have some studies reported relatively common isolated dendritic Ca2+ transients in CA1 pyramidal neurons while other studies, including voltage imaging studies, have reported the opposite?*

We thank the Reviewer for the opportunity to highlight a few important points regarding functional autonomy of dendrites based on the analysis of our model. We would like to first note that only parallel calcium and voltage imaging studies will be able to ultimately resolve this debate. Nevertheless, below we briefly summarize our take on this issue.

(1) In general, most Ca2+ imaging studies found that soma-independent dendritic events are rare. "Isolated dendritic transients (no coincident somatic event; see fig. S6, C and D, for example) were overall rare. Isolated apical dendritic Ca2+ transients, which have not previously been reported in CA1PNs, were larger and more frequent than those observed in basal dendrites." (O'Hare et al., 2022). "Activity in the ... basal dendrites ... along the track but outside of the place field was rarely observed" (Sheffield and Dombeck, 2014) and "overall, isolated dendritic transients were similar in size but occurred far less frequently than coincident dendrite-soma transients", or "data indicate that spatially reliable dendritic firing was almost exclusively yoked to somatic tuning, likely reflecting strong backpropagation of burst firing during traversals of the somatic PF" (Rolotti et al., 2022). Consistent with this observation, a dendritic Vm peak chosen randomly from any branch has ~93% probability to be related to a bAP in our model. However, it is also true that ~90% of events in the model are local events, simply because isolated events involve ~60-times fewer branches (1.8 on average) than events associated with bAPs (114 branches) in the model. If the spatial extent of typical local events are also similarly small in real neurons as in the model, then even rare occurrences of dendritic events may reveal substantial dendritic independence. We added a section quantifying the functional autonomy of dendrites in the model in the main text, around Fig 4H.

(2) Ca2+ indicators are slower and nonlinear and thus they are somewhat unreliable reporters of dendritic voltage events, especially in distal dendrites (Wu et al., 2026; Gonzalez et al., 2026). To illustrate this, we calculated three metrics in our model that were also reported in recent dendritic Ca2+ imaging studies (Rolotti et al., 2022, Sheffield et al., 2014, 2017). First, we calculated the fraction of bAPs detected in a branch (called dendrite-soma coupling in Rolotti et al., 2022, see their Fig. 2C) as a function of the distance of the branch from the soma (our new Fig. 4I). In the Ca2+ imaging data, this was essentially constant ~30%

between distances 5-100 μm from the soma. In contrast, the fraction of bAPs detected in the model was 100% in this range as bAPs propagation failures did not occur before μ100 μm. This is also consistent with a recent voltage imaging study showing that even low-transmission bAPs reliably propagate to the proximal dendrites (Lee et al., 2026, Fig 3G). The low and distance independent dendrite-soma coupling reported by Rolotti et al. can only be reconciled with the known biophysics of neurons if the recorded calcium signal is unreliable reporter of the underlying voltage. Indeed, it has been reported that Ca signals associated with bAPs can be absent in some dendritic branches (Landau et al., 2022) or that local, nonlinear Ca signals can appear in the absence of local regenerative voltage response (Weber et al., 2016, Tran-Van-Minh et al., 2016) and that the Ca signals are highly variable across cells (Eltes et al., 2019).

Second, we calculated the fraction of local events as a function of the distance from the soma (our Fig 4J; see also Fig. 2F in Rolotti et al.). When averaged across all branches, this was somewhat lower in the model (18%) than in the data (38%) which, again, could be explained by the low reliability of detecting global voltage events in all compartments based on the calcium signal.

Third, the range of branch-spike-prevalence (BSP) values in our model (0.5-0.9; Fig. 4H) seem consistent with that reported (0.4-0.8) at first (Fig 4C of Sheffield et al., 2014; Fig 2 of Sheffield et al., 2017). However, we note that there are several important differences: for technical reasons, Sheffield et al. reported BSP for place field traversals and not for individual events, and they measured Ca2+ dynamics in the basal dendrites. Since bAPs are almost always present in all basal dendrites in the model (basal BSP > 0.9 for all events with somatic spikes) and place field traversals were always accompanied by somatic APs, BSP for basal dendrites would be nearly 1 in the model. Thus, the lower BSP values reported by Sheffield et al. could be explained by the limited reliability of the Ca2+ indicators in reporting regenerative voltage events in neuronal processes.

We briefly discussed these differences in the Discussion (lines 474-478).

(3) Finally, to our knowledge, there are 3 relevant *in vivo* voltage imaging studies in CA1 PNs. Liao et al., 2024 found that in induced place cells the tuning of dendritic events (presumably local or back-propagating Na-spike) was similar to the somatic tuning, which is consistent with our model where dendritic activity and tuning is dominated by bAPs. However, they did not acquire simultaneous signals from the dendrites and the soma so they could not study the independence of the dendritic events. Lee et al. (2026) found that only 10% of the dendritic events are not associated with a somatic spike, which is lower than the number of independent events in the model. However, the events they found were generated in the distal apical trunk (their Fig 3D) and they could not record from the most distal branches where most of the isolated events were generated in our model. Gonzalez et al., 2026 measured voltage and calcium in selected locations within the dendritic tree, and could not reliably estimate the fraction of isolated events throughout the cell. (Gonzalez et al, 2024 measured voltage only in single spines and soma, but did not quantify independent dendritic events; Wong-Campos et al., 2023 measured dendritic integration and bAPs in L23 branches; Wu et al. 2026 recorded in CA2 neurons.)

We added a paragraph in the discussion comparing the level of functional autonomy present in the model dendrites to recent Ca- and voltage-imaging studies (lines 467-474).

> *Minor concerns:*
>
> *(1) Abstract:*

> *There is a need to explain what currentscape is - even at the cost of not invoking its name. To a reader not familiar with currentscape, the abstract is extremely difficult to understand.*

We reworded the title and the abstract to make them more accessible to readers not familiar with the term currentscape.

> *(2) "Currentscape analysis of place field dynamics" section:*
>
> *It would be helpful to emphasize upfront that dendritic determinants of individual somatic APs versus CSBs will be discussed separately. Since somatic action potentials are discussed before CSBs, I found this section initially confusing as I attributed those findings to CSBs until reading the next paragraph.*

We added a sentence to clarify that we analysed subthreshold responses, APs and CSBs separately.

> *(3) Bottom of p2 discussing mixed literature on what drives CSBs in CA1 PCs:*
>
> *Overall accurate and useful point, but an important nuance is glossed over which misportrays state of field. References ex vivo studies that fail to drive CSBs with somatic current injection and in vivo study successfully doing so. These aren't really conflicting results. In vivo current injection co-occurs with spontaneous synaptic input, which is high in CA1 and results in PCs that are significantly depolarized at rest relative to those in acute slices. Bittner 2017 ex vivo results are consistent with this: CSBs driven by Cs+-based internal solution to block K+ channels (partially, using strategy of purposefully high series resistance). Similar situation in vivo given that A-type K+ channels are inactivated by depol. Resulting increase in input resistance lowers input threshold to CSB. This is clarified in Results, p.5: "Under in vivo-like synaptic input conditions (see below and Methods), dendritic Ca2+-spikes could also be evoked by somatic current injection (Fig. S1E), as in Bittner et al. (2015).", which makes p. 2 feel especially awkward.*

We agree with the Reviewer that these are not necessarily conflicting results. We rephrased this section, emphasizing that the role of the different input pathways in the initiation of CSBs are not clear.

> *(4) Abbreviating "pyramidal neuron" with PC is confusing:*
>
> *PC often means place cell. The authors could change this, such that PC refers to "pyramidal cell", or else use PN as an abbreviation. It is important to avoid confusion, especially because place cell dynamics feature prominently in the manuscript.*

Thanks for the suggestion. We replaced PC with PN throughout the manuscript.

> *(5) Only apical dendritic parameters are described in section 2 of Results, but the full morphology is shown in Figure 3B with basal currents shown in panels C and F. Some clarification is needed - either what currents were considered for basal dendrites and why, or else why basal dendritic current parameters were not considered for this simulation using apical dendritic current injection but nonetheless examining basal dendritic currents.*

We clarified in the text that the original model contained a standard set of Na and K channels (line 178).

> *(6) Clarify "i" and "s" in the Figure 3C legend - "intrinsic" and "synaptic" white letterings are small/hard to see in the bottom subpanels.*

We now spell out intrinsic and synaptic in the Figure and increased the contrast of the letterings.

> *(7) Regarding the computational benefit of recursively decomposing axial currents along an adaptively truncated acyclic graph, it would be useful to (a) include a supplemental figure benchmarking this approach to standard approaches to quantify the described gain in computational efficiency and (b) describe computing hardware in the Methods.*

We included an estimated benefit of the pruning process (line 758) as well as the utilised computing hardware and the simulation times in the Methods (line 776).

> ***Reviewer #2 (Recommendations for the authors):***
>
> *The manuscript is in great shape, it is well organized, and the figures are gorgeous. I believe that the extended currentscape is a great extension of the original currentscape method. In particular, the possibility of partitioning currents by the spatial location of their sources is a great addition. >*
>
> *Recommendations:*
>
> *(1) The method is applied in the context of an interesting case study that highlights its usefulness. However, the model in the study is so complex that it is difficult to develop an intuition of how currents should be flowing, and this makes it hard to intuitively validate the visualization method. I think that applying the extended currentscape in a simpler model - maybe a soma with a dendrite with two branches, fewer compartments - would be instrumental in developing this intuition. >*

We now first use a simple model with a soma and a dendrite with two branches to introduce the concepts in Figure 2 and provide a few examples where the reader can compare the results with their own intuition in simpler cases. We also added the currentscape analysis of a standard, two-compartmental model from Pinsky and Rinzel, 1994 as Supplementary Figure 1.

> *(2) I found a number of typos and minor stylistic details you may want to fix in a revised version of the manuscript.*
>
> *(a) Abstractine, line 12. I believe the word "recursive" is a bit technical at this point. It's meaning in this context becomes clear after ones goes through the details of the algorithm (Figure 2). >*

We replaced the word “recursive” with “iterative”. We hope that this will make the abstract clearer for the readers. In fact, we realized that the word iterative is a better description of the algorithm, so we replaced the “recursive” with “iterative” consistently throughout the manuscript.

> *(b) Figure 1, caption."Since we included the capacitive current, the magnitude of the inward and the outward currents is identical (Kirchhoff's law)."This sentence can be confusing. If the inward and outward currents are the same, the membrane potential doesn't change. I believe that you are including the capacitive current in the inward (or outward) currents.*

Indeed, we included the capacitive current in the inward or outward currents. We changed the text to clarify this.

> *(c) Lines 92-93. I do not fully understand this sentence. Are you making an assumption? What does 'continuos flow of axial current' mean? >*

By ‘continuous flow of axial current’ we meant a spatially continuous stream of axial currents flowing from the reference to the target. To clarify this, we added the explanatory sentence: “i.e., if the axial current is not blocked or reversed between the reference and the target.”

> *(d) Equation (1.) Why summing axial currents over j? Is this for the case of a branching point?*

The compartment could be 1) part of a continuous segment of dendritic branch, where axial currents can flow from the distal and the proximal direction (sum over 2); 2) It can be a branch point with 3 axial currents; 3) or it can be a leaf compartment with only one axial current, in which case the summation is not relevant. We clarified this in the text.

> *(e) Figure 2, caption. Typo. "When the axial currents flows..." Should it be 'current'? - Figure 3, caption. Typo in (C) "Extended currentscape" >*

Corrected.

> *(f) Figure 4. I cannot see the grey lines or the dotted lines mentioned in the caption. >*

We added an arrow highlighting the gray and the dotted lines in the figure.

> *(g) Figure 5, caption. "Red boxes highlight regions analyzed in panels B-D."Because this is a spatially extended model, region may be confused with spatial location, but you are highlighting a temporal interval. >*

We rephrased the caption referring to temporal intervals now.

> *(h) Line 341. This is a numerical experiment, correct? >*

We clarified in the text and added that it was indeed a simulation experiment.

> *(i) Line 349. Should it be 'distributions'? >*

Corrected

> *(j) Line 422. Typo. Missing space 'in vivousing' >*

Corrected

> *(k) Line 537. "Preprocessing membrane..." I found this entire subsection a bit confusing and hard to read.*

We rephrased this subsection to clarify it and facilitate reading.

https://doi.org/10.7554/eLife.108352.2.sa0